[140] J. E. Rau, "Real-time complex spatial modulation," *J. Opt. Soc. Amer.*, vol. 57, p. 798, 1967.
[141] J. K. Hawkins and C. J. Munsey, "Image processing by electro-optical techniques," *J. Opt. Soc. Amer.*, vol. 57, p. 914, 1967.
[142] H. Arsenault and A. Boivin, "Optical filter synthesis by holographic methods," *J. Opt. Soc. Amer.*, vol. 58, p. 1490, 1968.
[143] J. P. Kirk and A. L. Jones, "Phase-only complex-valued spatial filter," *J. Opt. Soc. Amer.*, vol. 61, p. 1023, 1971.
[144] F. T. S. Yu and G. C. Kung, "Synthesis of optimum complex spatial filters," *J. Opt. Soc. Amer.*, vol. 62, p. 147, 1972.
[145] S. J. Krulikoski, Jr., D. C. Kowalski, and F. R. Whitehead, "Coherent optical parallel processing," *Bendix Tech. J.*, p. 59, 1968.
[146] B. M. Watrasiewicz, "Optical filtering," *Optics and Laser Tech.*, p. 288, 1972.
[147] A. A. Eschenfelder, "Promise of magneto-optic storage systems compared to conventional magnetic technology," *J. Appl. Phys.*, vol. 41, p. 1372, 1970.
[148] M. Arm and M. King, "Holographic storage of electric signals," *Appl. Opt.*, vol. 8, p. 1413, 1969.
[149] D. B. Fraser and J. R. Maldonado, "Improved aging and switching of lead zirconate-lead titanate ceramics with indium electrodes," *J. Appl. Phys.*, vol. 41, p. 2172, 1970.
[150] J. C. Urbach and R. W. Meier, "Thermoplastic xerographic holography," *Appl. Opt.*, vol. 5, p. 666, 1966.
[151] L. H. Lin and M. L. Beauchamp, "Write-read-erase in situ optical memory using thermoplastic holograms," *Appl. Opt.*, vol. 9, p. 2088, 1970.

Digital Reconstruction of Multidimensional Signals from Their Projections

RUSSELL M. MERSEREAU, MEMBER, IEEE, AND ALAN V. OPPENHEIM, SENIOR MEMBER, IEEE

Invited Paper

Abstract—**In a wide variety of applications it is necessary to infer the structure of a multidimensional object from a set of its projections. There has been a long-standing interest in this problem and a number of different techniques have been proposed. In this paper, we present a tutorial review of the reconstruction problem and some of the algorithms which have been proposed for its solution. In addition, we present a number of new algorithms that appear to have some advantages over previous algorithms. Some comparisons of these algorithms applied to reconstructions of two-dimensional pictures are given. Furthermore, a number of new theoretical results are presented relating to the minimum number of projections necessary for exact reconstruction.**

I. Introduction

IN A WIDE VARIETY of applications, it is necessary to infer the structure of a multidimensional object from a set of its projections. X-ray photographs, for example, represent two-dimensional projections of the irradiated three-dimensional structures. Details can be obtained from the projections considered collectively that are not apparent in any one of them alone. Similarly, transmission electron micrographs represent two-dimensional projections of the three-dimensional structures being examined. Other examples arise in the inversion of fan-beam radio-telescope scans and in the recovery of a point-spread function from a set of line spreads.

Because of its potential benefits to so many different fields, particularly medicine and molecular biology, there has been a long-standing interest in this problem, and a number of different techniques have been proposed. While some analog techniques have been considered, specifically optical methods, most of the techniques proposed are in part numerical and thus require the use of a digital computer. Typically, the computations involved are sufficiently complex that off-line processing is required. A part of the present interest in the problem appears to stem from an awareness that with the continuing trend toward faster, cheaper, digital computers and hardware it may soon be, and to a limited extent already is, possible to implement systems on-line for reconstruction from projections.

The techniques that exist for reconstruction fall into two basic classes—one in which the reconstruction is performed in normal signal space and one in which it is performed in Fourier space. While any technique can, of course, be interpreted and analyzed in either space or in both together, most techniques are more easily implemented in one space than the other. Whether implemented in signal space or Fourier space, the reconstruction algorithms can be conveniently interpreted by means of a straightforward and interesting theorem which we refer to as the projection-slice theorem. In essence this theorem states that the Fourier transform of a projection is a slice of the Fourier transform of the projected object. This theorem appears to have first been applied to the reconstruction problem in 1956 by Bracewell [1]. His interest involved the inversion of fan-beam radio-telescope scans. The algorithm proposed at that time was implemented in Fourier space. Although still based on the projection-slice theorem, a modified algorithm was later proposed by Bracewell and Riddle [2] which could be implemented entirely in signal space.

In 1968 DeRosier and Klug [3] proposed a Fourier space technique again based on the projection-slice theorem which was similar to, but apparently derived independently of, Bracewell's results. DeRosier and Klug were interested in the reconstruction problem primarily within the framework of molecular biology, where the projections obtained corresponded to

This invited paper is one of a series planned on topics of general interest—The Editor.

Manuscript received January 31, 1974; revised May 10, 1974. This work was supported in part by the Advanced Research Projects Agency monitored by ONR under Contract N-00014-67-A-0204-0064 and in part by the National Science Foundation under Grant GK-31353.

The authors are with the Department of Electrical Engineering and Research Laboratory of Electronics, Massachusetts Institute of Technology, Cambridge, Mass. 02139.

electron micrographs. They subsequently applied their method to a variety of virus structures and in many of the examples were able to take advantage of considerable symmetry in the structures studied. In 1971 Vainshtein [4] and Ramachandran and Lakshminarayanan [5], following DeRosier and Klug, formulated a signal-space algorithm similar to that proposed by Bracewell and Riddle.

An optical technique was used by Garrison *et al.* [6] for making reconstructions from medical X-rays. It implemented a variation of the Bracewell and Riddle algorithm optically. Fourier domain reconstructions from medical X-rays were also investigated by Tretiak, Ozonoff, Klopping, and Eden [7].

Another interesting set of approaches to the problem are the iterative algebraic techniques, implemented in signal space, by Herman [8], Gordon, Bender, and Herman [9], and Gilbert [10]. A new system for on-line radiographic analysis of the brain using reconstructions made by an iterative algebraic technique has recently been marketed [11]. It has proven useful for locating tumors and blood clots in the brain.

In this paper, we present a tutorial review of the reconstruction problem and some of the algorithms which have been proposed for its solution. In addition, we shall present a number of new algorithms that appear to have some advantages over previous algorithms. Furthermore, a number of new theoretical results will be presented relating to the minimum number of projections necessary for exact reconstruction. Mersereau has shown, in particular, that, taken at the right orientation, exact reconstruction can theoretically be carried out from a single projection [12], [13]. While, as will be discussed, this is not a practical algorithm for reconstruction because of the high sensitivity involved, it appears to be an important theoretical result. In particular, it provides one means for mapping multidimensional functions to one-dimensional functions and may have potential application to bandwidth compression and multidimensional digital filter design [14].

In Section II we discuss the theoretical background for understanding the reconstruction problem including the projection-slice theorem and in Section III we consider the question of the number of projections theoretically required for exact reconstruction. Section IV is concerned with a review of a variety of practical reconstruction algorithms which are conveniently interpreted, although not necessarily best implemented, in Fourier space. Section V considers some new modifications of these algorithms. In Section VI we discuss briefly several other algorithms including the iterative algebraic reconstruction techniques referred to earlier.

II. Theoretical Background

Although sometimes implemented in signal space, most of the reconstruction algorithms which will be discussed in subsequent sections are conveniently interpreted in terms of Fourier space and the projection-slice theorem. Thus in this section, we summarize briefly the N-dimensional continuous Fourier transform (CFT) for continuous variables and the N-dimensional discrete Fourier transform (DFT) for discrete variables. We shall then define projections and prove the projection-slice theorem.

A. The N-Dimensional Continuous Fourier Transform (CFT)

We consider here a function $f(x_1, x_2, \cdots, x_N)$ of N continuous variables $x_1, x_2, \cdots, x_N$. We will generally find it convenient to express the N-tuple $(x_1, x_2, \cdots, x_N)$ as a vector $\boldsymbol{x}$ and refer to the function as $f(\boldsymbol{x})$. The N-dimensional Fourier transform of $f(\boldsymbol{x})$ is denoted by $F(\omega_1, \omega_2, \cdots, \omega_N)$ or $F(\boldsymbol{\omega})$. The domain of $f(\boldsymbol{x})$ will be referred to as signal space and the domain of $F(\boldsymbol{\omega})$ as Fourier space. The N-dimensional function $f(\boldsymbol{x})$ and its Fourier transform are related by

$$F(\omega_1, \omega_2, \cdots, \omega_N) = \int_{-\infty}^{+\infty} \cdots \int_{-\infty}^{+\infty} f(x_1, x_2, \cdots, x_N) \exp\left[-j(\omega_1 x_1 + \omega_2 x_2 + \cdots + \omega_N x_N)\right] dx_1 dx_2 \cdots dx_N \quad (1)$$

$$f(x_1, x_2, \cdots, x_N) = \frac{1}{(2\pi)^N} \int_{-\infty}^{+\infty} \cdots \int_{-\infty}^{+\infty} F(\omega_1, \omega_2, \cdots, \omega_N) \cdot \exp\left[j(\omega_1 x_1 + \omega_2 x_2 + \cdots + \omega_N x_N)\right] d\omega_1 d\omega_2 \cdots d\omega_N \quad (2)$$

or, expressed in vector notation,

$$F(\boldsymbol{\omega}) = \int_{-\infty}^{+\infty} f(\boldsymbol{x}) \exp\left[-j(\boldsymbol{x} \cdot \boldsymbol{\omega})\right] d\boldsymbol{x} \quad (3)$$

and

$$f(\boldsymbol{x}) = \frac{1}{(2\pi)^N} \int_{-\infty}^{+\infty} F(\boldsymbol{\omega}) \exp\left[j(\boldsymbol{x} \cdot \boldsymbol{\omega})\right] d\boldsymbol{\omega} \quad (4)$$

where $\boldsymbol{x} \cdot \boldsymbol{\omega}$ denotes the dot product of the vectors $\boldsymbol{x}$ and $\boldsymbol{\omega}$ or equivalently with $\boldsymbol{x}$ and $\boldsymbol{\omega}$ interpreted as row matrices, $\boldsymbol{x} \cdot \boldsymbol{\omega} = \boldsymbol{x}\boldsymbol{\omega}^t$.

A useful property of the N-dimensional Fourier transform pair which we will want to use later is the fact that if $f(\boldsymbol{x})$ and $F(\boldsymbol{\omega})$ form a Fourier transform pair, then $f(\boldsymbol{x}A)$ and $F(\boldsymbol{\omega}A)$ form a Fourier transform pair if A is an orthogonal matrix, i.e., $A^t = A^{-1}$.

This property is easily verified by direct substitution into (3). Thus an orthogonal transformation or equivalently an orthogonal change of coordinates in signal space results in the same change of coordinates in Fourier space. For example, for $N = 2$, if

$$A = \begin{bmatrix} \cos\theta & \sin\theta \\ -\sin\theta & \cos\theta \end{bmatrix} \quad (5)$$

so that $f(\boldsymbol{x})$ is rotated by an angle θ, then its Fourier transform will be rotated by the same angle θ.

B. The N-Dimensional Discrete Fourier Transform (DFT)

We shall generally be interested in functions which can be processed by a digital computer and consequently can be represented by their samples. Thus we consider the class of band-limited functions. Specifically, $f(\boldsymbol{x})$ is said to be band-limited if there exists an N-tuple $(W_1, W_2, \cdots, W_N)$ such that $F(\boldsymbol{\omega})$ is zero for $|\omega_i| > W_i$, $i = 1, 2, \cdots, N$. The N-tuple W will be referred to as the vector bandwidth. In some cases it is convenient to set $W = \max(W_1, W_2, \cdots, W_N)$ and refer to the scalar W as the bandwidth of $f(\boldsymbol{x})$.

The N-dimensional sampling theorem states that if $f(\boldsymbol{x})$ is sampled in signal space on a rectangular lattice with the sample spacing in dimension x_i less than π/W_i, then $f(\boldsymbol{x})$ can be recovered from its samples. Sampling on a rectangular lattice will be referred to as periodic Cartesian sampling.

Let us denote by $g(n)$ the N-dimensional sequence corresponding to sampling $f(x)$ with a sample spacing of π/V_i in the dimension x_i where $V_i > W_i$ so that

$$g(n_1, n_2, \cdots, n_N) = f\left\{\frac{\pi n_1}{V_1}, \frac{\pi n_2}{V_2}, \cdots, \frac{\pi n_N}{V_N}\right\}. \tag{6}$$

From the sampling theorem the Fourier transform $F(\omega)$ of $f(x)$ can be obtained from $g(n)$ by the relation

$$F(\omega) = \frac{\pi^N}{V_1 V_2 \cdots V_N}\left\{\sum_{n=-\infty}^{+\infty} g(n) \exp\left[-j\pi(n \cdot \omega_V)\right]\right\} \cdot b_V(\omega) \tag{7}$$

where ω_V denotes the vector $\left(\frac{\omega_1}{V_1}, \frac{\omega_2}{V_2}, \cdots, \frac{\omega_N}{V_N}\right)$ and

$$b_V(\omega) = \begin{cases} 1, & |\omega_i| < V_i, \quad i = 1, 2, \cdots, N \\ 0, & \text{otherwise.} \end{cases}$$

Likewise, the sequence $g(n)$ can be obtained from $F(\omega)$ by the relation

$$g(n) = \frac{1}{(2\pi)^N} \int_{-V}^{V} F(\omega) \exp\left\{j\pi(n \cdot \omega_V)\right\} d\omega. \tag{8}$$

The original N-dimensional function $f(x)$ can be obtained from the sequence $g(n)$ by means of the interpolation formula

$$f(x) = \sum_{n=-\infty}^{+\infty} g(n)\, \phi(n, x) \tag{9}$$

where

$$\phi(n, x) = \prod_{i=1}^{N} \frac{\sin V_i\left(x_i - \frac{n_i \pi}{V_i}\right)}{V_i\left(x_i - \frac{n_i \pi}{V_i}\right)}. \tag{10}$$

When only a finite number of the samples of $f(x)$ are nonzero, the Fourier transform $F(\omega)$ can be represented by a finite set of Cartesian samples. The relationship between the Cartesian samples of $F(\omega)$ and the Cartesian samples of $f(x)$ is the N-dimensional DFT. Specifically, let us assume that

$$g(n) = 0, \quad \text{if } n_i \geqslant M_i \text{ or } n_i < 0, \quad i = 1, 2, \cdots, N.$$

We now consider the Cartesian samples of $F(\omega)$, which we denote by $G(k)$ given by

$$G(k_1, k_2, \cdots, k_N) = \frac{\pi^N}{V_1 V_2 \cdots V_N} \cdot F\left(\frac{2V_1}{M_1} k_1, \frac{2V_2}{M_2} k_2, \cdots, \frac{2V_N}{M_N} k_N\right)$$

where k_i is an integer such that

$$-\frac{M_i}{2} + 1 \leqslant k_i \leqslant \frac{M_i}{2}, \quad \text{if } M_i \text{ is even}$$

$$-\frac{M_i - 1}{2} \leqslant k_i \leqslant \frac{M_i - 1}{2}, \quad \text{if } M_i \text{ is odd.}$$

Then

$$G(k_1, k_2, \cdots, k_N) = \sum_{n_1=0}^{M_1-1} \cdots \sum_{n_N=0}^{M_N-1} g(n_1, n_2, \cdots, n_N) \cdot \exp\left[-j2\pi\left(\frac{k_1 n_1}{M_1} + \frac{k_2 n_2}{M_2} + \cdots + \frac{k_N n_N}{M_N}\right)\right] \tag{11}$$

and

$$g(n_1, n_2, \cdots, n_N) = \frac{1}{M_1 \cdot M_2 \cdots M_N} \cdot \sum_{k_1} \cdots \sum_{k_N} G(k_1, k_2, \cdots, k_N) \cdot \exp\left[j2\pi\left(\frac{k_1 n_1}{M_1} + \cdots + \frac{k_N n_N}{M_N}\right)\right]. \tag{12}$$

Since $G(k_1, k_2, \cdots, k_N)$ as defined in (11) is periodic in k_i it is frequently convenient to use the values of k_i in the range $0 \leqslant k_i \leqslant M_i - 1$ rather than over the ranges given above. Adopting this convention and defining the vector $\boldsymbol{k}_M$ as the N-tuple

$$\left(\frac{k_1}{M_1}, \frac{k_2}{M_2}, \cdots, \frac{k_N}{M_N}\right)$$

we can express (11) and (12) as

$$G(k) = \sum_{n=0}^{M-1} g(n) \exp\left\{-j2\pi(n \cdot \boldsymbol{k}_M)\right\} \tag{13}$$

and

$$g(n) = \frac{1}{M_1 M_2 \cdots M_N} \sum_{k=0}^{M-1} G(k) \exp\left\{j2\pi(n \cdot \boldsymbol{k}_M)\right\}. \tag{14}$$

Equations (13) and (14) are referred to as the N-dimensional DFT pair. The N-dimensional DFT can be computed efficiently by using the one-dimensional fast Fourier transform (FFT) algorithm, since the summations in (13) and (14) can each be decomposed as a cascade of one-dimensional transforms.

The class of functions $f(x)$ which can be represented by a finite number of samples will be referred to as band-limited functions of finite order M where

$$M = \max\left\{M_1, M_2, \cdots, M_N\right\}.$$

C. Projections

A projection is a mapping of an N-dimensional function to an $(N-1)$-dimensional function obtained by integrating the function in a particular direction. For example, $p_{x_2}(x_1)$ given by

$$p_{x_2}(x_1) = \int_{-\infty}^{+\infty} f(x_1, x_2)\, dx_2 \tag{15}$$

is an example of a projection of the two-dimensional function $f(x_1, x_2)$ onto one dimension.

For the general case, we define a projection as follows: Let $f(x)$ denote an N-dimensional function and let u denote a new set of coordinates where

$$x = uA$$

and A is an orthogonal transformation. Then a projection

onto the hyperplane $(u_1, u_2, \cdots, u_{i-1}, u_{i+1}, \cdots, u_N)$ is defined as

$$p_{u_i}(u_1, u_2, \cdots, u_{i-1}, u_{i+1}, \cdots, u_N) = \int_{-\infty}^{\infty} f(uA)\, du_i. \tag{16}$$

The coordinate axis u_i, which is normal to the hyperplane onto which $f(x)$ is projected, will be referred to as the projection axis.

For $N = 2$, the matrix A is given by

$$A = \begin{bmatrix} \cos\theta & \sin\theta \\ -\sin\theta & \cos\theta \end{bmatrix}.$$

In this case, the u_1, u_2 coordinate axes are offset from the (x_1, x_2) axes by an angle of θ. For two-dimensional functions it will generally be convenient to refer to a projection by its angle θ. A projection at angle θ will be interpreted to mean a projection onto the coordinate u_1, which is at an angle θ with x_1. Equivalently, then, the *projection axis* u_2 is at an angle θ to the coordinate axis x_2. Equation (15) corresponds to a projection at an angle $\theta = 0$ or equivalently with x_2 as the projection axis.

D. The Projection-Slice Theorem

The projection-slice theorem relates the $(N-1)$-dimensional Fourier transforms of the projections to the N-dimensional Fourier transform of the original function. Basically, the theorem states that the $(N-1)$-dimensional Fourier transform of a projection is a "slice" through the N-dimensional Fourier transform of $f(x)$.

First, let us consider a projection for which the projection axis is one of the coordinate axes of $f(x)$, for example, x_1. Then $p_{x_1}(x_2, \cdots, x_N)$ is given by

$$p_{x_1}(x_2, \cdots, x_N) = \int_{-\infty}^{+\infty} f(x)\, dx_1 \tag{17}$$

and its $(N-1)$-dimensional Fourier transform is given by

$$P_{x_1}(\omega_2, \cdots, \omega_N) = \int_{-\infty}^{+\infty} \cdots \int_{-\infty}^{+\infty} p_{x_1}(x_2, \cdots, x_N) \cdot \exp\left[-j(\omega_2 x_2 + \cdots + \omega_N x_N)\right]. \tag{18}$$

Comparing (18) and (1), we see that

$$P_{x_1}(\omega_2, \cdots, \omega_N) = F(\omega_1, \omega_2, \cdots, \omega_N)\big|_{\omega_1 = 0}. \tag{19}$$

In other words, $P_{x_1}(\omega_2, \cdots, \omega_N)$ is a "slice" of $F(\omega_1, \omega_2, \cdots, \omega_N)$ defined by $\omega_1 = 0$. Clearly, a projection whose axis is any coordinate axis x_i has a Fourier transform that is a slice of $F(\omega_1, \omega_2, \cdots, \omega_N)$ defined by $\omega_i = 0$.

A general projection was defined in (16) where A is an orthogonal transformation. It was argued previously that if $F(\omega)$ is the Fourier transform of $f(x)$ then $F(\Omega)$ is the Fourier transform of $f(u)$ where

$$x = uA$$
$$\omega = \Omega A. \tag{20}$$

From this, (19) is easily generalized to state that a projection for which the projection axis is the transformed coordinate u_i has an $(N-1)$-dimensional Fourier transform which is a slice of $F(\Omega)$ for $\Omega_i = 0$ where the coordinate systems u and Ω are related to the coordinate systems x and ω by the same orthogonal transformation. In two dimensions, for example, the projection-slice theorem states that the one-dimensional Fourier transform of a projection at an angle θ is a slice at the same angle of the two-dimensional Fourier transform of the original object. This relationship is depicted in Fig. 1.

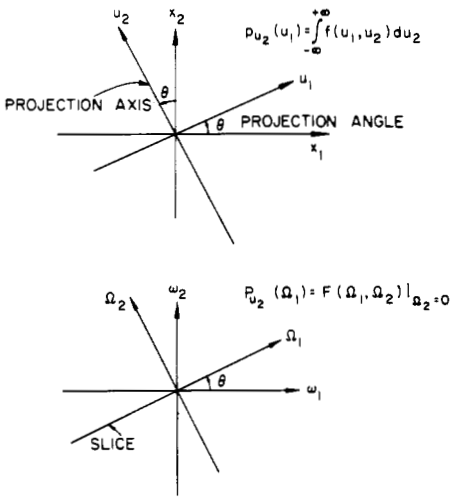

Fig. 1. The relationship between the projection of a two-dimensional function and the slice of its Fourier transform.

E. The Basis for Reconstruction from Projections

From the projection-slice theorem, we see that specification of a projection in signal space corresponds to the specification of a slice in Fourier space and thus represents a partial specification of the signal itself. In principle, then, if an unlimited number of projections at different orientations are available, the Fourier transform of $f(x)$ can be obtained and therefore so can $f(x)$ itself. Generally, in any practical context, we are restricted to a finite number of projections.

Under certain assumptions, it is possible to carry out exact reconstruction from a finite number of projections. If the structure is highly symmetrical, for example, a finite number of projections might suffice for exact reconstruction. For example, for a two-dimensional circularly symmetric function all of its projections are identical and consequently such a function can be represented exactly by a single projection. Similarly, in three dimensions, for an object which is cylindrically symmetric all of the projections for which the projection axis is normal to the longitudinal axis are identical and consequently, in this case also, a single projection is sufficient. Helical objects can also be often reconstructed from a single projection.

In Section III we shall consider another class of functions that can be represented by a finite number of projections.

In utilizing projections for reconstruction, many of the algorithms involve computing the Fourier transforms of the projections. The Fourier transform of each projection is a function of a set of continuous variables, but only a finite number of points from each Fourier transform can be computed and stored. Thus from the projections, only samples in the Fourier domain are available, in part because of the limited number of projections and in part because only samples of the Fourier transform on each slice can be obtained. The essence of the reconstruction problem, then, is to approximate all of Fourier space from its values on a discrete point set.

F. Reduction of the Dimensionality of the Reconstruction Problem

As we saw in Section II-E, the underlying basis for reconstruction is to obtain samples in the Fourier plane by transforming projections. Intuitively it seems reasonable that projections need not be taken in all orientations. For three-dimensional objects, for example, we could imagine using only projections in the spatial domain on planes parallel to one of the coordinate axes, say x_1. Slices of these projections at $x_1 = A$ are then projections of the two-dimensional function $f(A, x_2, x_3)$ and, consequently, a two-dimensional reconstruction algorithm can be applied to reconstructing this two-dimensional slice of the three-dimensional object. In this way, the three-dimensional object can be built up slice by slice and, consequently, the three-dimensional problem can be reduced to a series of two-dimensional problems. In the general case, we can apply a similar argument to reduce an N-dimensional problem to a set of $(N-1)$-dimensional problems each of which can in principle be reduced to an $(N-1)$-dimensional problem, etc.

Thus in principle, an N-dimensional problem can be reduced to a set of two-dimensional problems. Often this procedure requires considerably less storage and is simpler computationally than attacking the N-dimensional problem directly. Furthermore, in many cases, we may be content with very coarse sampling in one or several dimensions. For the three-dimensional problem, for example, reconstruction of only a few slices may be sufficient.

In the next sections, we discuss a number of reconstruction theorems and algorithms. The discussion will be phrased in terms of reconstructing two-dimensional functions from their one-dimensional projections. This is motivated by a number of considerations. Notationally and mathematically, the two-dimensional problem is easier to express and all of the results presented easily generalize to the N-dimensional case. Furthermore, as we discussed above, an N-dimensional problem can be reduced to a set of two-dimensional reconstruction problems and for most practical examples, this is an efficient procedure computationally.

III. Exact Reconstruction from a Finite Number of Projections

The exact reconstruction of an arbitrary signal requires an infinite number of projections, since an infinite number of slices are required to encompass all of Fourier space. If, however, the unknown signal is known to have some underlying mathematical form, then exact reconstructions can often be performed from a limited set of projections. For example, as indicated previously, if the unknown is circularly symmetric then all of its projections are necessarily identical and $f(x_1, x_2)$ can be recovered from any one of them. Similarly, if $f(x_1, x_2)$ is separable so that it is of the form $f(x_1, x_2) = g(x_1)h(x_2)$ then it can be reconstructed from the two projections taken normal to the coordinate axes. This follows from the fact that in this case $p_{x_1}(x_2)$ is proportional to $h(x_2)$ and $p_{x_2}(x_1)$ is proportional to $g(x_1)$. The classes of circularly symmetric or separable functions do not represent very general classes of signals. There is, however, a class of functions that are somewhat more general and that can, in principle, be reconstructed from a finite number of projections. This is the class of band-limited functions of finite order, i.e., the class of functions that can be specified by a finite number of Cartesian samples. This class is very general, as evidenced by the fact that most signals processed digitally are assumed to be of this class since they are represented digitally by a finite number of samples. In this section, we consider the possibility of exact reconstruction from a finite number of projections for this class of signals. While the results do not lead to practical reconstruction algorithms they emphasize the underlying structure in this class of problems.

Throughout the discussion we will assume that the unknown signal can be represented by a square raster of samples M points on a side. We could, of course, assume with more generality that we have a rectangular raster of M_1 samples in one dimension and M_2 samples in the orthogonal dimension. None of our results would be substantially changed although the introduction of an additional parameter would have made the expressions slightly more complex. Seeing no particular reason (theoretical or practical) for introducing this additional parameter, we have chosen not to do so.

A. The One-Projection Theorem [12]

An important property of band-limited functions of finite order is that they can be represented by a single projection, as discussed below. This theorem will be referred to as the one-projection theorem.

Theorem (One-Projection Theorem): Let A and B denote two positive or negative integers and m, m', n, and n' integers in the range $0 \leq m, n, m', n' \leq M-1$. A band-limited function $f(x_1, x_2)$ of bandwidth W and order M can be represented exactly by a single projection at angle $\theta = \tan^{-1}(A/B)$ if A and B have no common factors and if $Bm + An = Bm' + An'$ only for $m = m'$ and $n = n'$.

The angle θ for such a projection will be referred to as a critical angle and the corresponding slice of $F(\omega_1, \omega_2)$ will be referred to as a critical slice.

Proof: Since the function is band-limited, it is sufficient to determine its samples on a Cartesian raster, i.e., to determine the samples $f((m\pi/W), (n\pi/W))$ for $0 \leq (m, n) \leq M-1$. From (7), the Fourier transform $F(\omega_1, \omega_2)$ of $f(x_1, x_2)$ is expressed in terms of these samples as

$$F(\omega_1, \omega_2) = \frac{\pi^2}{W^2} \sum_{m=0}^{M-1} \sum_{n=0}^{M-1} f\left(\frac{m\pi}{W}, \frac{n\pi}{W}\right) \cdot \exp\left[-j\frac{\pi}{W}(m\omega_1 + n\omega_2)\right] b_W(\omega) \quad (21)$$

where

$$b_W(\omega) = \begin{cases} 1, & |\omega| \leq \dfrac{W\sqrt{A^2+B^2}}{\max[|A|, |B|]} \\ 0, & \text{otherwise.} \end{cases} \quad (22)$$

Now consider a slice of $F(\omega_1, \omega_2)$ denoted by $S_\theta(\omega)$, at angle θ, corresponding to the one-dimensional Fourier transform of the projection at that angle. With ω representing frequency along the slice, the slice is specified by

$$\omega_1 = \omega \cos\theta$$

$$\omega_2 = \omega \sin\theta$$

so that

$$S_\theta(\omega) = F(\omega\cos\theta, \omega\sin\theta). \quad (23)$$

Thus with

$$\theta = \tan^{-1} \frac{A}{B}$$

$$S_\theta(\omega) = \frac{\pi^2}{W^2} \sum_{m=0}^{M-1} \sum_{n=0}^{M-1} f\left(\frac{m\pi}{W}, \frac{n\pi}{W}\right) \cdot \exp\left[-j \frac{\pi}{W} \frac{\omega}{\sqrt{A^2 + B^2}} (Bm + An)\right] b_W(\omega). \quad (24)$$

We observe that for

$$|\omega| \leq \frac{W\sqrt{A^2 + B^2}}{\max [|A|, |B|]}$$

(24) corresponds to a one-dimensional polynomial of the form

$$p(z) = a_Q z^Q + a_{Q-1} z^{Q-1} + \cdots + a_R z^R \quad (25)$$

where

$$z = \exp\left[-j \frac{\pi\omega}{W\sqrt{A^2 + B^2}}\right] \quad (26)$$

$$Q = \max (Bm + An), \qquad 0 \leq m, n \leq M - 1$$

and

$$R = \min (Bm + An), \qquad 0 \leq m, n \leq M - 1.$$

R can, and in general will, be negative. The polynomial $p(z)$ is specified by $[(|A| + |B|)(M - 1) + 1]$ coefficients or equivalently by $[(|A| + |B|)(M - 1) + 1]$ samples. Thus it will be convenient to refer to $p(z)$ as a polynomial of degree $[(|A| + |B|)(M - 1)]$.

It is clear from (24) that $p(z)$, or equivalently $S_\theta(\omega)$, has at most M^2 nonzero coefficients. Under the stated conditions on A and B, we note that the coefficients of the polynomial $p(z)$ are the function samples $f((m\pi/W), (n\pi/W))$. If the slice $S_\theta(\omega)$ is completely specified then all of its coefficients, and hence the function samples, can be found. Consequently, the stated conditions represent sufficient conditions for $f(x_1, x_2)$ to be represented exactly by a single projection. If the stated conditions are not met then at least one of the coefficients in $p(z)$ will consist of a sum of two or more function samples and the number of nonzero coefficients in $p(z)$ will be reduced accordingly. In this case then, the function samples cannot be uniquely recovered from the polynomial coefficients. This completes the proof of the theorem.

At this point, a comment should be made on the degrees of the polynomials corresponding to the different critical slices. The preceding theorem has shown that there are an infinite number of critical slices. Each corresponds to a polynomial of degree at least $M^2 - 1$, since there are M^2 nonzero function samples and thus M^2 nonzero coefficients that each such polynomial must contain. There is no maximum degree for these polynomials. For example, consider the slice at $\theta = \tan^{-1} 1/2M$. From our theorem this is seen to be a critical slice and it corresponds to a polynomial of degree $2M^2 - M - 1$. Of the $2M^2 - M$ coefficients that it contains, however, only M^2 are nonzero; $M^2 - M$ of the coefficients are identically zero. On the other hand, the slice at angle $\theta = \tan^{-1} 1/M$ corresponds to a polynomial of degree $M^2 - 1$. Since there are M^2 function samples, no critical slice can be a polynomial of degree less than $M^2 - 1$ and thus $\theta = \tan^{-1} 1/M$ represents an optimum in the sense that of all the critical slices this one is of minimum degree.

To obtain the function samples from the slice polynomial we must first obtain a sufficient number of samples of $S_\theta(\omega)$, the number of samples required being one plus the degree of the polynomial. The samples can be obtained by sampling the projection above its Nyquist rate and performing the appropriate DFT computation. For example, when $\theta = \tan^{-1} 1/M$, M^2 such samples are needed. When the slice samples are obtained from the DFT, they will be equally spaced along the slice and they will extend along the entire nonzero frequency band. Since for this example the width of this band is $2W\sqrt{M^2 + 1}/M$, the frequency spacing between adjacent samples is

$$\Delta\omega = \frac{2W}{M^3} \sqrt{M^2 + 1}. \quad (27)$$

Thus substituting in (24), the values of the M^2 samples are

$$S_{\theta_0}(k\Delta\omega) = \frac{\pi^2}{W^2} \sum_{m=0}^{M-1} \sum_{n=0}^{M-1} f\left(\frac{m\pi}{W}, \frac{n\pi}{W}\right) \cdot \exp\left[-j \frac{2\pi k}{M^3} (Mm + n)\right], \qquad k = -\frac{M^2}{2} + 1, \cdots, 0, 1, \cdots, \frac{M^2}{2}. \quad (28)$$

For notational simplicity, let us define

$$g(mM + n) = f\left(\frac{m\pi}{W}, \frac{n\pi}{W}\right).$$

This mapping of a two-dimensional sequence to a one-dimensional sequence is unambiguous because of the limited ranges of m and n. Then setting $p = mM + n$, (28) can be expressed as

$$S_{\theta_0}(k\Delta\omega) = \frac{\pi^2}{W^2} \sum_{p=0}^{M^2-1} g(p) \exp\left[-j \frac{2\pi kp}{M^3}\right], \qquad k = -\frac{M^2}{2} + 1, \cdots, \frac{M^2}{2}. \quad (29)$$

Equation (28) or equivalently (29) is in principle invertible so that the M^2 function samples $g(p)$ can be computed from M^2 samples of the critical slice. In practice, however, this set of equations is nearly impossible to invert. In particular, assume that the slice samples $S_{\theta_0}(k\Delta\omega)$ are not known exactly due to measurement errors, quantization effects, model inaccuracies, etc. If the observed slice samples are $S_{\theta_0}(k\Delta\omega) + \epsilon(k)$ where $\epsilon(k)$ is a random sequence with zero mean and for which

$$E[\epsilon(k)\epsilon(l)] = 0, \qquad k \neq l \quad (30)$$

$$E[\epsilon^2(k)] = \sigma^2 \quad (31)$$

where $E[\cdot]$ denotes the expected value, then with $\delta(p)$ denoting the error in $g(p)$ due to the error $\epsilon(k)$, it has been shown [12] that $\delta(p)$ has zero mean and

$$E[\delta^2(p)] \simeq \frac{\sigma^2}{M^4} \left(\frac{2Me}{\pi}\right)^{2M^2-2}. \quad (32)$$

For $M = 256$, $\log [\delta^2/\sigma^2]$ is more than 10^6 bits, indicating that the inversion of (29) is extremely ill-conditioned for any but very small values of M.

The problems involved in reconstructing band-limited functions of order M are computational ones and are due to the

high orders of the polynomials involved. This is unavoidable, since to recover all M^2 samples from a single projection, it is necessary to work with a polynomial of degree greater than $M^2 - 1$.[1] If, however, we are willing to use more than one projection, then we can work with lower degree polynomials. This procedure can perhaps be best explained in terms of an example.

Let us consider a band-limited picture of order 4 which we wish to reconstruct from the two projections at $\theta_1 = \tan^{-1} \frac{1}{2}$ and $\theta_2 = \tan^{-1} -\frac{1}{2}$. Since each of these slices has a rational slope, each corresponds to a polynomial of finite degree. In this case the degree is 9 and thus

$$\begin{aligned} S_{\theta_1}(k\Delta\omega) &= f(0,0) + f(0,1)E_k + [f(0,2) + f(1,0)]\,E_k^2 \\ &\quad + [f(0,3) + f(1,1)]\,E_k^3 + [f(1,2) \\ &\quad + f(2,0)]\,E_k^4 + [f(1,3) + f(2,1)]\,E_k^5 \\ &\quad + [f(2,2) + f(3,0)]\,E_k^6 + [f(2,3) \\ &\quad + f(3,1)]\,E_k^7 + f(3,2)E_k^8 + f(3,3)E_k^9 \\ &= \sum_{i=0}^{9} a_i E_k^i \end{aligned} \tag{33}$$

where

$$E_k = \exp\left[-j\,\frac{2\pi k}{20}\right].$$

Similarly we can write

$$\begin{aligned} S_{\theta_2}(k\Delta\omega) &= f(0,3)E_k^{-3} + f(0,2)E_k^{-2} + f[(0,1) + f(1,3)]\,E_k^{-1} \\ &\quad + [f(0,0) + f(1,2)] + [f(2,3) + f(1,1)]\,E_k \\ &\quad + [f(2,2) + f(1,0)]\,E_k^2 + [f(2,1) + f(3,3)]\,E_k^3 \\ &\quad + [f(2,0) + f(3,2)]\,E_k^4 + f(3,1)E_k^5 + f(3,0)E_k^6 \\ &= \sum_{i=0}^{9} b_i E_k^{i-3}. \end{aligned} \tag{34}$$

If $S_{\theta_1}(k\Delta\omega)$ and $S_{\theta_2}(k\Delta\omega)$ are each available for 10 different evenly spaced values of k then we can obtain the two sequences a_i and b_i. From these we can compute the function samples by

$$\begin{array}{llll} f(0,0) = a_0 & f(1,0) = a_2 - b_1 & f(2,0) = b_7 - a_8 & f(3,0) = b_9 \\ f(0,1) = a_1 & f(1,1) = a_3 - b_0 & f(2,1) = b_6 - a_9 & f(3,1) = b_8 \\ f(0,2) = b_1 & f(1,2) = b_3 - a_0 & f(2,2) = a_6 - b_9 & f(3,2) = a_8 \\ f(0,3) = b_0 & f(1,3) = b_2 - a_1 & f(2,3) = a_7 - b_8 & f(3,3) = a_9. \end{array}$$

The technique for performing a reconstruction from more than one projection, following this approach, can be summarized in the following steps:

1) find a sufficient set of slice angles;
2) sample the slices at $d + 1$ points, where d is the degree of the polynomial along each slice, and compute the coefficients corresponding to these polynomials;
3) set up a system of linear equations relating the polynomial coefficients to the function samples;
4) solve this set of equations to obtain the Nyquist samples of the unknown;
5) use the band-limited interpolation formula (9) and (10) to recover $f(x, y)$ from its Nyquist samples.

None of these steps is particularly simple. In our example, we reconstructed from the slices at $\theta_1 = \tan^{-1} \frac{1}{2}$ and $\theta_2 = \tan^{-1} -\frac{1}{2}$. Had we instead chosen to work with the slices at $\theta_1 = \tan^{-1} \frac{1}{2}$ and $\theta_2 = \tan^{-1} 2$, which are of the same degrees, we would not have been able to solve the resulting linear equations. We must, therefore, be careful when we choose a set of slice angles to insure that the resulting equations are solvable. This is difficult to do for large M since the number of equations and the number of variables grow as M^2. It can be shown that the projections at $\theta_1 = \tan^{-1} 2/M$ and $\theta_2 = \tan^{-1} -2/M$ are sufficient to reconstruct a function of order M, although from (32) we see that for $M > 4$ it is difficult to determine the coefficients of the resulting polynomials. It can also be shown that an 8×8 array can be reconstructed from the four projections $\theta_1 = \tan^{-1} \frac{1}{2}$, $\theta_2 = \tan^{-1} 2$, $\theta_3 = \tan^{-1} -\frac{1}{2}$, $\theta_4 = \tan^{-1} - 2$. In all of these cases the resulting linear equations are straightforward to compute.

From the orders of the polynomials involved and (32), we can perhaps infer that to reconstruct an $M \times M$ picture will require on the order of $M/2$ projections by these techniques, due to the sensitivity problems, alluded to earlier, associated with the coefficient calculations. Since for large values of M this requires formidable matrix manipulations, it is perhaps reasonable to consider alternative reconstruction procedures which, using simpler algorithms, will produce good quality reconstructions from roughly the same number of projections. This we will do in the next section. Before doing so, however, we wish to close this section with a discussion of a somewhat different procedure for reconstructing exactly a band-limited function of finite order M from a set of $M + 1$ projections. While this procedure is also somewhat difficult to implement exactly, it forms the basis for an approximate procedure to be discussed in Section V that appears to be among the most successful.

To develop the exact reconstruction procedure we again consider $f(x, y)$ to be band-limited with bandwidth W and of finite order M. Then

$$F(\omega_1, \omega_2) = \frac{\pi}{W^2} \sum_{m=0}^{M-1} \sum_{n=0}^{M-1} f\left(\frac{m\pi}{W}, \frac{n\pi}{W}\right) z_1^m z_2^n\, b_W(\omega_1, \omega_2)$$

where

$$z_1 = \exp\left(-j\,\frac{\pi}{W}\,\omega_1\right) \quad \text{and} \quad z_2 = \exp\left(-j\,\frac{\pi}{W}\,\omega_2\right).$$

Thus over the region of support ($|\omega_1| \leqslant W$, $|\omega_2| \leqslant W$), $F(\omega_1, \omega_2)$ corresponds to a two-dimensional polynomial of degree $M - 1$ in each of the complex variables z_1 and z_2. Along horizontal (ω_1 constant) or vertical (ω_2 constant) lines in the Fourier plane, $F(\omega_1, \omega_2)$ varies as a one-dimensional polynomial of degree $M - 1$ in either z_1 or z_2. Therefore, if $F(\omega_1, \omega_2)$ is known at any M points along any horizontal or vertical line in the Fourier plane (subject to the constraint that the points all must lie within the region of support) it is known at all points on that line. Now consider a slice at an arbitrary angle θ in the Fourier plane. Since $f(x_1, x_2)$ is constrained to be band-limited, $S_\theta(\omega) = 0$ for $|\omega| \geqslant W_\theta$ where

$$W_\theta = \frac{W}{\max\{|\cos\theta|, |\sin\theta|\}} \tag{35}$$

[1] A similar result was obtained by Smith *et al.* [15] for a slightly different class of functions.

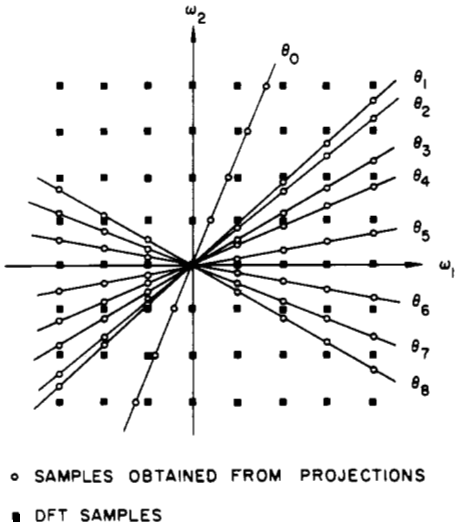

Fig. 2. The set of Fourier plane samples from which an 8 by 8 picture can be reconstructed exactly under the assumption that the picture is band-limited and of order 8.

is the bandwidth of the projection at this particular angle. Thus we can expand the projection in terms of its samples according to (36).

$$p_\theta(u) = \sum_{n=-\infty}^{\infty} p_\theta\left(\frac{n\pi}{W_\theta}\right) \frac{\sin \frac{W_\theta}{\pi}\left(u - \frac{n\pi}{W_\theta}\right)}{\frac{W_\theta}{\pi}\left(u - \frac{n\pi}{W_\theta}\right)}. \tag{36}$$

Now suppose that we limit θ to fall in the range $-(\pi/4) \leqslant \theta \leqslant (\pi/4)$ and we evaluate the value of the slice function at M equally spaced points from the sampled projection. Thus (36) becomes

$$S_\theta\left(\frac{2Wk}{M\cos\theta}\right) = \frac{\pi\cos\theta}{W} \sum_{n=-\infty}^{\infty} p_\theta\left(\frac{n\pi\cos\theta}{W}\right) \cdot \exp\left[-j\frac{2\pi}{M}nk\right], \quad k = -\frac{M}{2}+1, \cdots, \frac{M}{2}. \tag{37}$$

If this is done for M different angles in the range $-(\pi/4) \leqslant \theta_i \leqslant (\pi/4)$ then $F(\omega_1, \omega_2)$ will be known at an array of sample locations such as that illustrated in Fig. 2 for $M = 8$. Included in the same figure are locations for the M^2 DFT samples of $f(x_1, x_2)$. It should be noted that M vertical lines can be drawn through the slice samples and that the DFT samples lie along these same vertical lines. Therefore, from our earlier statement, it is seen that all of the DFT samples, except for those which lie along the line $\omega_x = 0$, are completely determined from the raster of slice samples. If, however, in addition we know M slice samples of a slice whose angle falls outside the range $[-(\pi/4), (\pi/4)]$, denoted by θ_0 in Fig. 2, then by interpolating along horizontal lines in the Fourier plane we can determine the DFT samples along the line $\omega_1 = 0$, since along each horizontal line we now know $F(\omega_1, \omega_2)$ at M points: $M - 1$ from the previously computed DFT points and 1 from this last projection. Thus all M^2 samples of $F(\omega_1, \omega_2)$ that correspond to its DFT can be determined from $M + 1$ projections and these samples, in turn, completely specify $F(x_1, x_2)$. This procedure for exact reconstruction basically involves one-dimensional polynomial interpolation. In Section V we shall consider an approximation of this interpolation procedure. First, however, we consider in the next section approximate reconstruction from a polar raster.

IV. Approximate Reconstructions from a Polar Raster

Since specification of a projection in signal space corresponds to specification of a slice in Fourier space, if all the projections for a continuous range of angles $0 \leqslant \theta \leqslant \pi$ are known, the entire Fourier space is swept out and consequently the function is known exactly. Conversely, if only a finite number of projections are known, an arbitrary function cannot be specified exactly, since its Fourier transform is constrained only on a finite set of slice lines and is elsewhere merely constrained to be infinitely differentiable. If $F(\omega_1, \omega_2)$ is expressed in polar coordinates as $\mathcal{F}(\omega, \theta)$ then, substituting into the inverse Fourier transform integral,

$$f(x_1, x_2) = \frac{1}{(2\pi)^2} \int_{-\infty}^{+\infty} \int_0^{\pi} \mathcal{F}(\omega, \theta) \cdot \exp\left[j(x_1\omega\cos\theta + x_2\omega\sin\theta)\right] |\omega| \, d\omega d\theta \tag{38}$$

or, since $\mathcal{F}(\omega, \theta)$ for fixed θ is the slice of $F(\omega_1, \omega_2)$ at angle θ,

$$f(x_1, x_2) = \frac{1}{(2\pi)^2} \int_{-\infty}^{+\infty} \int_0^{\pi} S_\theta(\omega) \cdot \exp\left[j(x_1\omega\cos\theta + x_2\omega\sin\theta)\right] |\omega| \, d\omega d\theta. \tag{39}$$

Equation (39) tells us how $f(x_1, x_2)$ can be reconstructed from its projections. In general, however, to apply (39), an infinite number of slices are needed, while in practice only a finite number will be available. Thus in general, (39) must be approximated from the values of $S_\theta(\omega)$ at only a finite number of discrete angles. Intuitively, one would expect that as the number of projections used for the reconstruction increases, the accuracy of the reconstruction, or more specifically, the resolution of detail in the reconstructed image will increase. This is basically a consequence of the fact that the slices $S_\theta(\omega)$ sample the two-dimensional Fourier transform at only a finite number of discrete angles. Some attempts to quantify the relationship between the number of projections and the resulting resolution available in the reconstruction are discussed in [2], [16]-[18].

In addition to requiring an infinite number of slices, (39) also requires that each slice be specified for all values of ω. This is, in general, impossible to do because the Fourier transforms which must be computed to determine the slices of $F(\omega_1, \omega_2)$ must be computed digitally. If the projections are all band-limited, which is the case if $f(x_1, x_2)$ is band-limited because of the projection-slice theorem, then samples of $S_\theta(\omega)$ can be computed by applying the DFT to samples of the projection $p_\theta(u)$. With a finite set of equally spaced values of θ, and with samples of $S_\theta(\omega)$ equally spaced in ω computed from the projections, we obtain a set of samples of $\mathcal{F}(\omega, \theta)$ on a regular polar raster as indicated in Fig. 3. The first set of approximate algorithms to be considered will be those utilizing such a set of samples, although they are not all implemented in the Fourier plane.

Before addressing the problem of reconstructing from this raster, however, let us briefly consider some issues associated

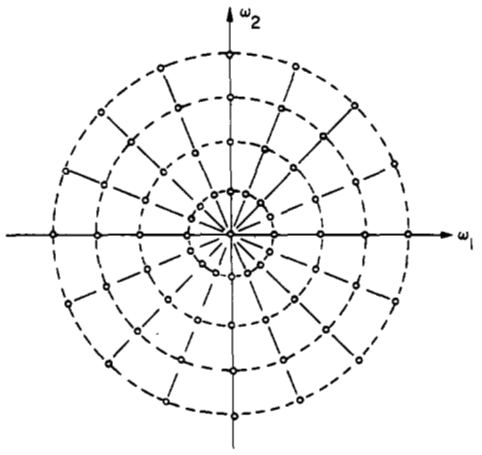

Fig. 3. Polar raster indicating the set of points at which a two-dimensional Fourier transform will be known from 8 projections with the Fourier transforms computed digitally.

with obtaining these polar samples. The radius of the polar raster is, of necessity, finite and thus only a limited portion of the Fourier plane can be directly sampled. It thus follows that if $f(x_1, x_2)$ can be reconstructed from such a raster then the remainder of the Fourier plane either is unimportant in specifying $f(x_1, x_2)$ or is completely determined by the samples in the raster. We shall assume the former situation—that $f(x_1, x_2)$ is either band-limited or very nearly band-limited and that the polar raster samples the entire nonzero frequency region. Therefore, we shall assume that $F(\omega_1, \omega_2)$ is nonzero only over a bounded region of the Fourier plane that can be enclosed by a circle of radius $\sqrt{2}\,W$. Each projection then corresponds to a band-limited one-dimensional function with bandwidth less than $\sqrt{2}\,W$ so that if each is periodically sampled with an intersample distance less than $\pi/\sqrt{2}\,W$ (meters) no information will be lost.

Each sampled projection represents a sequence of numbers of infinite duration. We can obtain M samples of the slice corresponding to a particular projection by converting that infinitely long sequence to an M point sequence by aliasing. Thus if

$$\left\{p_\theta\left(\frac{\pi}{\sqrt{2}\,W}n\right),\quad n=-\infty,\cdots,-1,0,1,\cdots,\infty\right\}$$

represents the infinitely long sequence and we define

$$\tilde{p}_\theta(n)=\sum_{m=-\infty}^{\infty}p_\theta\left(\frac{\pi}{\sqrt{2}\,W}(Mm+n)\right),\qquad n=0,1,\cdots,M-1 \tag{40}$$

then $\tilde{p}_\theta(n)$ is a sequence of length M whose DFT corresponds to evenly spaced samples of the Fourier transform of $p_\theta(u)$. In practice, of course, the sum in (40) must be performed using finite limits. If this procedure is followed for each of the N projections that are evenly spaced in angle over the range 0 to π, then we will know the Fourier transform $F(\omega_1, \omega_2)$ on a regular polar raster such as that in Fig. 3.

If $f(x_1, x_2)$ is band-limited and of order M then it is completely specified by its $M \times M$ point DFT. If it is not of finite order, then it can hopefully be approximately determined by its DFT. Since the DFT corresponds to samples of $F(\omega_1, \omega_2)$ on a Cartesian raster, one possible reconstruction algorithm is to interpolate from the known samples on a polar raster to estimate the samples on a Cartesian raster, perform an inverse DFT, and use the result as an estimate of samples on a Cartesian raster of the unknown. This is the basis for the first set of approximate algorithms that we shall consider.

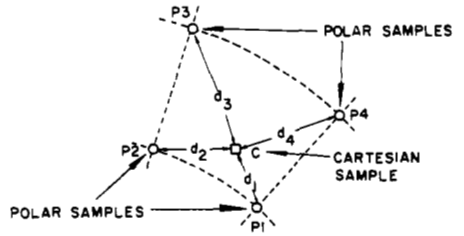

Fig. 4. Parameters for the definition of zeroth-order and linear interpolation.

To perform the necessary interpolation we may consider the use of a simple form of polynomial interpolation. Two interpolation techniques have been used—zeroth-order and linear interpolation. Each of these approximations is shown in Fig. 4. With zeroth-order interpolation, each Cartesian (DFT) sample is assigned the value of the nearest polar sample, whereas with linear interpolation it is assigned a weighted average of the four nearest polar values, the weighting varying inversely with the Euclidean distance between the Cartesian sample and the polar sample in question. In particular, for the Cartesian sample c indicated in Fig. 4, with $d_1 = \min[d_1, d_2, d_3, d_4]$, for zeroth-order interpolation we choose $F(c) = F(P1)$. With linear interpolation, $F(c)$ is computed as

$$F(c)=\frac{\frac{1}{d_1}F(P1)+\frac{1}{d_2}F(P2)+\frac{1}{d_3}F(P3)+\frac{1}{d_4}F(P4)}{\frac{1}{d_1}+\frac{1}{d_2}+\frac{1}{d_3}+\frac{1}{d_4}}. \tag{41}$$

The reconstruction algorithm can thus be summarized in the following steps:

1) Compute the Fourier transform of the sampled projections using a one-dimensional DFT to obtain a collection of sampled slices of $F(\omega_1, \omega_2)$ which represents a polar sampling of $F(\omega_1, \omega_2)$.

2) Use zeroth-order or linear interpolation to estimate the Cartesian samples of $F(\omega_1, \omega_2)$ which correspond to the DFT of a two-dimensional sequence

$$\left\{f\left(\frac{m\pi}{W},\frac{n\pi}{W}\right),\quad 0\leq m,n\leq M-1\right\}.$$

3) Estimate

$$\left\{f\left(\frac{m\pi}{W},\frac{n\pi}{W}\right),\quad 0\leq m,n\leq M-1\right\}$$

using a two-dimensional inverse DFT.

4) Approximate $f(x_1, x_2)$ as

$$\hat{f}(x_1,x_2)=\sum_{m=0}^{M-1}\sum_{n=0}^{M-1}f\left(\frac{m\pi}{W},\frac{n\pi}{W}\right)\cdot\frac{\sin\frac{W}{\pi}\left(x-\frac{m\pi}{W}\right)\sin\frac{W}{\pi}\left(y-\frac{n\pi}{W}\right)}{\frac{W^2}{\pi^2}\left(x-\frac{m\pi}{W}\right)\left(y-\frac{n\pi}{W}\right)}. \tag{42}$$

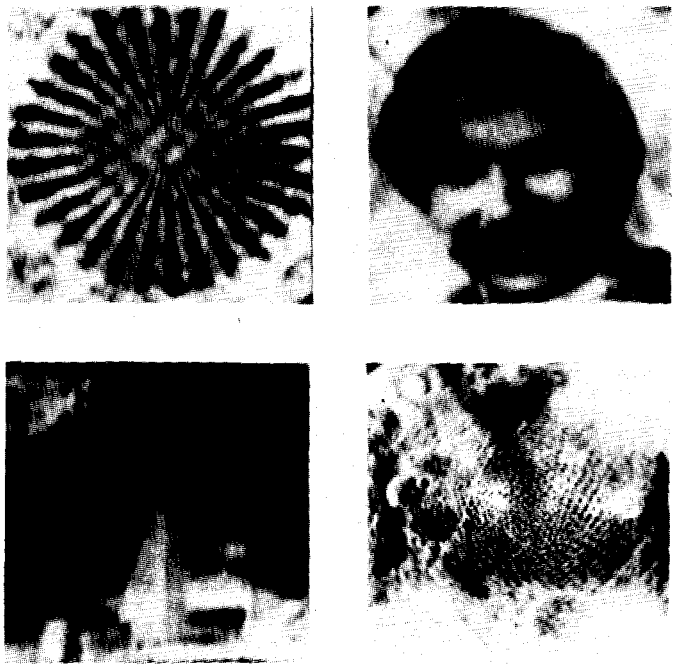

Fig. 5. Reconstruction of the pictures of Fig. 7 from their projections using zeroth-order interpolation from a polar raster.

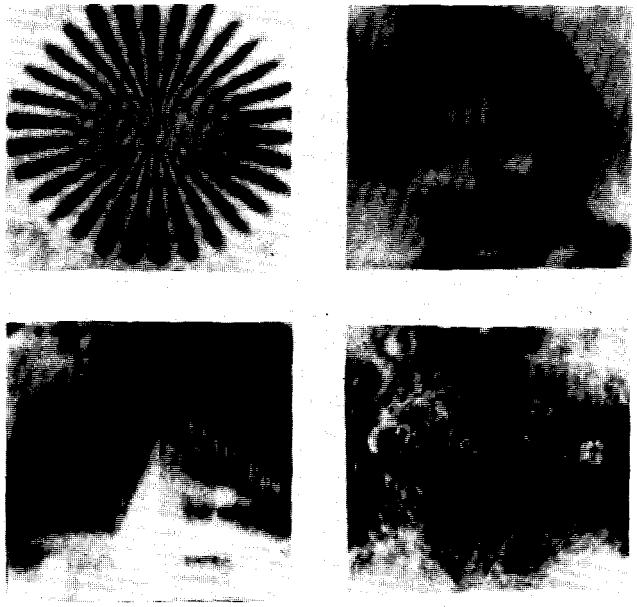

Fig. 6. Reconstruction of the pictures of Fig. 7 from their projections using linear interpolation from a polar raster.

For the interpolation to be effective, the Fourier transform must be reasonably smooth. Thus each projection should be considered as a two-sided sequence with its origin at the center. Choosing the origin at one of the end points of the projection introduces a linear phase component into the Fourier transform which will seriously impair the quality of the resulting reconstructions.

Figs. 5 and 6 present some reconstructions obtained by using the above technique with zeroth-order and linear interpolation, respectively.[2] Each of these reconstructions was

[2] All of the reconstructions presented in this paper were performed on a Digital Equipment Corporation PDP-9 computer with 24 000 words of core memory using 18-bit fixed-point arithmetic.

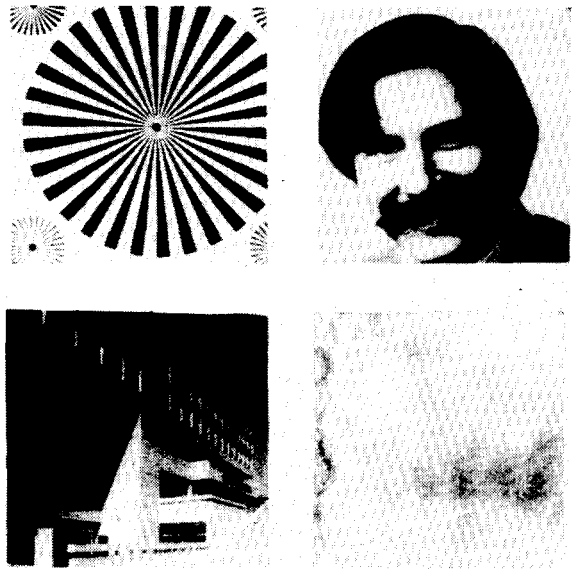

Fig. 7. Four original pictures for which the reconstruction from projections is to be carried out using a variety of algorithms.

made from 64 computer-generated projections equally spaced in angle, with each projection represented by 256 samples. The original pictures from which these projections were computed are included for comparison in Fig. 7. Discrepancies between the reconstructions and the originals are due to two distinct factors—errors made in computing the projections themselves, and errors introduced in performing the reconstructions. All of the reconstructions performed in this section were performed from the same set of projections and thus any comparison between different algorithms which reconstruct from a polar raster is dependent on only the latter type of error. In computing the projections it was assumed that the original photographs represented two-dimensional band-limited functions of order M, where the DFT computed in the reconstruction algorithms was of dimension $M \times M$.

A cursory examination of Figs. 5 and 6 reveals that the quality of the final reconstruction is very much dependent upon the method of interpolation which was used, although neither set of reconstructions is as good, perhaps, as one might wish. The reconstructions performed using linear interpolation seem preferable to those performed using zeroth-order interpolation. This is certainly reasonable since if $F(\omega_1, \omega_2)$ is continuous and slowly varying, one would expect the error from a piecewise planar approximation to be less than that from a piecewise constant approximation.

One of the possible explanations for the errors that were introduced by these algorithms is that insufficient projections were taken for linear interpolation to approximate accurately the entire Fourier plane. Indeed, it was noted experimentally, as expected, that as the number of projections was increased, the quality of the resulting reconstructions improved. Taking an increasing number of projections is impossible, however, in many practical situations because this requires more X-rays, more electron micrographs (a specimen can be destroyed by too much electron bombardment), etc. Another possibility to improve reconstruction quality is to use higher order interpolation algorithms, but this involves a major computational effort and would significantly add to the total computation time required. A third alternative, which is closely related, would be to augment the set of projections with additional projections computed from the given ones by some computationally ef-

ficient scheme, and then from this larger set of projections the linear interpolation algorithm can then be applied as before. Were these extra projections computed from the original set by linear or zeroth-order interpolation, then our reconstructions would be identical to those of the previous section, but by using some other interpolation scheme different and (it is hoped) improved reconstructions might be obtained. This is the central idea behind an algorithm which we refer to as the polar expansion algorithm.

Let us assume that $F(\omega_1, \omega_2)$ can be expanded in the form

$$F(\omega \cos\theta, \omega \sin\theta) = \mathcal{F}(\omega, \theta) = \sum_{m=-\infty}^{\infty} \sum_{n=-\infty}^{\infty} f_{mn}\, \Psi_{mn}(\omega, \theta) \tag{43}$$

where ω and θ are polar coordinate variables and where

$$\Psi_{mn}(\omega, \theta) = \exp\left[j\left(\frac{2\pi m\omega}{\sqrt{2}\,W} + n\theta\right)\right] b_W(\omega) \tag{44}$$

$$b_W(\omega) = \begin{cases} 1, & 0 \leqslant \omega < \sqrt{2}\,W \\ 0, & \text{otherwise.} \end{cases} \tag{45}$$

This choice is made because the set $\{\Psi_{mn}(\omega, \theta)\}$ is complete over the set of band-limited functions with bandwidth $\sqrt{2}\,W$ and a finite subset of the set should be capable of producing a good approximation to most unknowns.

In order to compute the coefficients f_{mn} of (43) we require an infinite number of projections. If, however, we approximate $\mathcal{F}(\omega, \theta)$ by a truncated expansion

$$\mathcal{F}(\omega, \theta) \simeq \sum_{m=-M_1/2+1}^{M_1/2} \sum_{n=-M_2/2+1}^{M_2/2} f_{mn} \cdot \exp\left[j\left(\frac{2\pi m\omega}{\sqrt{2}\,W} + n\theta\right)\right] b_W(\omega) \tag{46}$$

the coefficients f_{mn} can be computed efficiently from a finite number of projections using the DFT. In particular, we recognize that with f_{mn} viewed as a two-dimensional Cartesian sequence, (46) corresponds to its two-dimensional Fourier transform. By inserting finite limits in (46) we assumed that f_{mn} is of finite order. Consequently, the two-dimensional DFT of f_{mn} corresponds to samples of $\mathcal{F}(\omega, \theta)$ equally spaced in ω and equally spaced in θ. Hence f_{mn} can be obtained from these samples by means of the inverse DFT relation, i.e.,

$$f_{mn} = \frac{1}{M_1 M_2} \sum_{a=0}^{M_1-1} \sum_{b=0}^{M_2-1} \mathcal{F}\left(\frac{\sqrt{2}\,W}{M_1} a, \frac{2\pi}{M_1} b\right) \cdot \exp\left[-j2\pi\left(\frac{ma}{M_1} + \frac{nb}{M_2}\right)\right] \tag{47}$$

where

$$\mathcal{F}\left(\frac{\sqrt{2}\,W}{M_1} a, \frac{2\pi}{M_2} b\right), \quad a = 0, 1, \cdots, M-1 \text{ and } b = 0, 1, \cdots, M_2 - 1$$

correspond to samples of $F(\omega_1, \omega_2)$ on a regular polar raster formed by taking the $2M_1 - 1$ point DFT's of $M_2/2$ evenly spaced projections. From the coefficients $\{f_{mn}\}$ we can calculate the values of $F(\omega_1, \omega_2)$ along any other slices we wish using the expansion of (46). In particular, to obtain samples of $F(\omega_1, \omega_2)$ on a polar raster with M_4 rays of M_3 samples each, (46) becomes

$$\mathcal{F}\left(\frac{\sqrt{2}\,W}{M_3} k, \frac{2\pi}{M_4} l\right) = \sum_{m=-M_3/2+1}^{M_3/2} \sum_{n=-M_4/2+1}^{M_4/2} f_{mn} \cdot \exp\left[j\left(\frac{2\pi mk}{M_3} + \frac{2\pi nl}{M_4}\right)\right]. \tag{48}$$

Incorporating (47) we can thus arrive at a formula for interpolating the values of these extra slices. Specifically

$$\mathcal{F}\left(\frac{\sqrt{2}\,W}{M_3} k, \frac{2\pi}{M_4} l\right) = \sum_{a=0}^{M_1-1} \sum_{b=0}^{M_2-1} \mathcal{F}\left(\frac{\sqrt{2}\,W}{M_1} a, \frac{2\pi}{M_2} b\right) \cdot \exp\left[-j\pi\left(\frac{k}{M_3} - \frac{a}{M_1} + \frac{l}{M_4} - \frac{b}{M_2}\right)\right] \cdot \frac{\sin \pi M_1\left(\frac{k}{M_3} - \frac{a}{M_1}\right) \sin \pi M_2\left(\frac{l}{M_4} - \frac{b}{M_2}\right)}{M_1 M_2 \sin \pi\left(\frac{k}{M_3} - \frac{a}{M_1}\right) \sin \pi\left(\frac{l}{M_4} - \frac{b}{M_2}\right)} PW(\omega), \quad -\frac{M_3}{2} + 1 \leqslant k \leqslant \frac{M_3}{2} \quad -\frac{M_4}{2} + 1 \leqslant l \leqslant \frac{M_4}{2}. \tag{49}$$

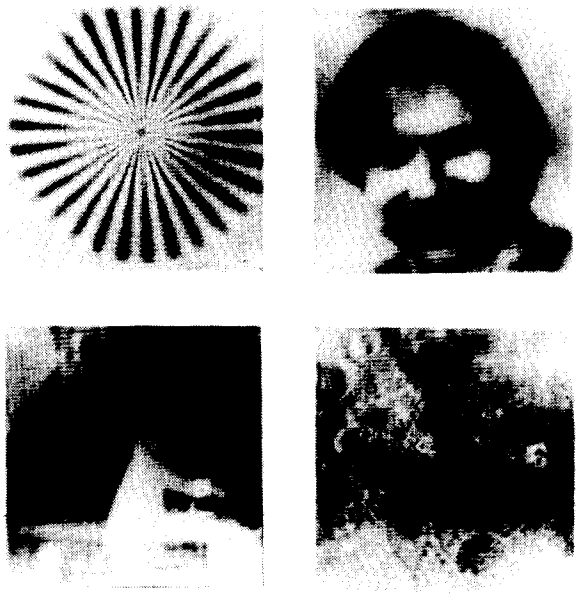

Fig. 8. Reconstruction of the pictures of Fig. 7 from their projections using the polar expansion algorithm.

Fig. 8 shows some reconstructions that were made from 64 original projections of 256 points each. Using the above techniques, 256 projections of 256 points apiece were then computed according to (48). Linear interpolation was then used to estimate the 256 X 256 DFT of the unknown, and an inverse 256 X 256 point DFT was performed. On the basis of these restricted examples it might be inferred that this algorithm yields slightly improved reconstructions compared with simple linear interpolation. This algorithm is quite similar to one

presented by DeRosier and Moore [19] using Hankel transformations, as discussed in Section VI of this paper. Their algorithm as used by themselves and others has been quite successful at reconstructing viruses, which do exhibit such symmetries.

Both algorithms which have been presented thus far have been based on interpolating from a polar raster to a Cartesian raster and then using the DFT to obtain samples of the original function. An alternative class of algorithms is based on a direct approximation of (39) using a two-dimensional extension of the trapezoidal rule. In particular, let us approximate

$$S_\theta(\omega)\exp\{j\omega(x\cos\theta + y\sin\theta)\} = g(\theta,\omega)$$

by a piecewise planar function that is planar over the "rectangular" region bounded by two radii and two circular sections. Assume that slices are known at angles $\theta_0, \theta_1, \cdots, \theta_{N-1}$ (not necessarily evenly spaced) and that along each slice the values of $S_{\theta_i}(\omega)$ are known at the R_1 values (R_1 even) designated by $\Omega[-(R_1/2)+1], \cdots, \Omega_0, \Omega_1, \cdots, \Omega_{R_1}/2$. Since these samples will presumably be computed from sampled projections using a DFT, we shall assume that the radial samples are evenly spaced and that

$$\Omega_{i+1} - \Omega_i = \Delta\omega = \frac{2\sqrt{2}\,W}{R_1}. \tag{50}$$

The angular spacing shall be designated by

$$\Delta\theta_i = \begin{cases} \theta_{i+1} - \theta_i, & i = 0, 1, \cdots, R_2 - 2 \\ \theta_0 - \theta_{R_2-1} + \pi, & i = R_2 - 1. \end{cases}$$

It should be noted that $\sum_{i=0}^{R_2-1}\Delta\theta_i = \pi$ and that if the projections are evenly spaced $\Delta\theta_i = \pi/R_2$. Referring then to Fig. 9, we can approximate $g(\theta,\omega)$ for $\theta_i \leqslant \theta \leqslant \theta_{i+1}, \Omega_k \leqslant \omega \leqslant \Omega_{k+1}$ by the planar section

$$g(\theta,\omega) \simeq A + B(\omega - \Omega_k) + C(\theta - \theta_i) + D(\omega - \Omega_k)(\theta - \theta_1) \tag{51}$$

where

$$A = g(\theta_i, \Omega_k)$$

$$B = \frac{g(\theta_i, \Omega_{k+1}) - g(\theta_i, \Omega_k)}{\Delta\omega}$$

$$C = \frac{g(\theta_{i+1}, \Omega_k) - g(\theta_i, \Omega_k)}{\Delta\theta_i}$$

$$D = \frac{g(\theta_{i+1}, \Omega_{k+1}) - g(\theta_{i+1}, \Omega_k) - g(\theta_i, \Omega_{k+1}) + g(\theta_i, \Omega_k)}{\Delta\omega\Delta\theta_i}.$$

By doing this for all sections, (39) becomes

$$f(x_1,x_2) \simeq \frac{2W^2}{3R_1^2\pi} S_{\theta_0}(0) + \frac{2W^2}{R_1^2\pi^2}\sum_{i=0}^{R_2-1}\Delta\theta_i \sum_{k=-R_1/2+1}^{R_1/2} |k| \cdot S_{\theta_i}\left(\frac{2\sqrt{2}\,kW}{R_1}\right)\exp\left\{j\frac{2\sqrt{2}\,kW}{R_1}(x_1\cos\theta_i + x_2\sin\theta_i)\right\}. \tag{52}$$

Equation (52) represents a reconstruction algorithm since it expresses $f(x_1,x_2)$ in terms of $S_\theta(k\Delta\omega)$, the slice samples. The direct computation of (52) is difficult as that equation is written. However, we can reinterpret it and use the DFT to make it easier to compute. Reinterpreting (52) has multiple advantages. It results in a straightforward computational procedure for implementing the algorithm, provides us with some insight into how the algorithm works, and shows us that this algorithm is equivalent to another algorithm—the so-called smearing algorithm which can be implemented in the space domain. With the smearing algorithm, each projection is back-projected or smeared in the direction of the original projection and the smeared projections are then weighted and summed. Let us define what is meant by smearing. If $p_{\theta_i}(u_i)$ represents the projection of $f(x,y)$ at angle θ_i where

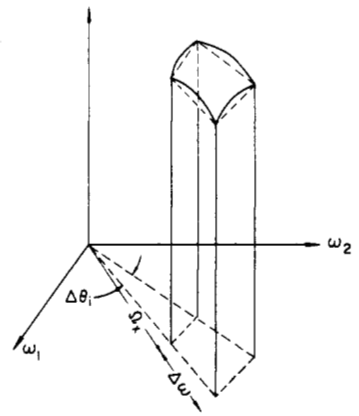

Fig. 9. Approximation of $g(\theta,\omega)$ by a planar section.

$$u_i = x_1\cos\theta_i + x_2\sin\theta_i$$
$$v_i = -x_1\sin\theta_i + x_2\cos\theta_i \tag{53}$$

then the smeared projection at angle θ_i, $p_{\theta_i}(u_i, v_i)$, is defined by

$$p_{\theta_i}(u_i, v_i) = p_{\theta_i}(u_i). \tag{54}$$

To express (52) in terms of smeared projections, we can first rewrite it as

$$f(x_1,x_2) \simeq \hat{f}(x_1,x_2) = \frac{2W^2}{3\pi R_1^2} S_{\theta_0}(0) + \frac{2W^2}{\pi^2 R_1^2}\sum_{i=0}^{R_2-1}\Delta\theta_i g_i(x_1,x_2) \tag{55}$$

where

$$g_i(x_1,x_2) = \sum_{k=-R_1/2+1}^{R_1/2} |k|\, S_{\theta_i}(k\Delta\omega) \cdot \exp\left[jk\Delta\omega\,(x_1\cos\theta_i + x_2\sin\theta_i)\right]. \tag{56}$$

If we define $\hat{g}_i(u_i, v_i) = g_i(x, y)$ with a change of coordinates, then

$$\hat{g}_i(u_i, v_i) = \sum_{k=-R_1/2+1}^{R_1/2} |k|\, S_{\theta_i}(k\Delta\omega)\exp\left[jku_i\Delta\omega\right]. \tag{57}$$

From (57) we see that $\hat{g}(u_i, v_i)$ is a function only of u_i and that it is thus a smeared quantity. Furthermore, the quantity that is smeared is a filtered projection. This filtering can be accomplished by computing the DFT of the projection, multiplying the resulting sequence by $|k|$, and then inverse transforming. According to (56), these filtered smeared projections $\{g_i(x_1, x_2)\}$ are then weighted, summed, and added to the dc bias (constant) function.

Instead of computing $\hat{g}_i(u_i)$ from $p_{\theta_i}(u_i)$ by computing transforms, we could confine ourselves totally to the space

domain and express $\hat{g}_i(u_i)$ as a (circular) convolution of $p_{\theta_i}(u_i)$ and the inverse DFT of $|k|$. This computation is cumbersome, however, and the modification of the projections is more easily carried out in the frequency domain than by performing the convolution in the space domain. Ramachandran and Lakshminarayanan [5] and Shepp and Logan [21] have shown, however, that by modifying the weighting function slightly, the convolution is more conveniently done directly than by using Fourier transforms.

This algorithm has been used by Bracewell [1], Vainshtein [22], Ramachandran [23], Herman [8], Gilbert [24], and perhaps others, with minor variations. There are a number of nice features to it. First, it imposes no requirements on $f(x_1, x_2)$ except that it be nearly band-limited and that $F(\omega_1, \omega_2)$ be "slowly varying" in ω_1 and ω_2 so that our original approximation of an integral by a sum is valid. These are not severe restrictions to impose. Another advantage of the algorithm is that the entire procedure can be implemented in the space domain (although, as we have seen, it may be more efficient to filter the projections in the frequency domain). Omitting the modification of the projections, this system can, in fact, be implemented optically and such an optical system has been built by Garrison, Grant *et al.* [6], [25]. Another feature of this algorithm, actually the nicest feature of all, is that it yields very good reconstructions.

There are, on the other hand, several problems inherent in use of the smearing algorithm. One of the most serious is that the reconstructions are very sensitive to inaccuracies in the input projections. Any error or "noise" in the projection is amplified in the reconstructions and, as a result, the final reconstructions appear noisy; that is, the reconstructions have a mottled or speckled appearance.

Some reconstructions formed by using this algorithm are shown in Figs. 10 and 11. In Fig. 10 several photographs are reconstructed from 64 projections—the projections that were used for the preceding algorithms. In Fig. 11 reconstructions are shown for 16, 32, 64, and 128 projections. It will be noted that for the example chosen the degradation with a decrease in the number of projections is serious. Such a degradation is to be expected but it is particularly serious for this example. It is informative to compare these reconstructions with those produced by linear interpolation. The smearing reconstructions clearly display more resolved details, although they do have a grainy or speckled appearance due to the noise mentioned earlier. A possible explanation is due to the fact that with the linear interpolation algorithm, the values of Cartesian samples of $F(\omega_1, \omega_2)$ were estimated from neighboring polar samples prior to performing an inverse DFT. As a result, polar samples which were not close to Cartesian samples were ignored. For large values of ω (the radial variable in a polar coordinate system) this effect is negligible since almost all of these polar samples are used, but for polar samples close to the origin this effect becomes significant, especially since for photographs, $|F(\omega_1, \omega_2)|$ is largest for those values of ω_1 and ω_2 near the origin. On the other hand, the smearing algorithm uses all of the information contained in the polar samples since all of the projections are treated identically.

The noise which is introduced in the smearing reconstructions is due to the high-frequency emphasis filter that is applied to the projections and it introduces computational errors similar to those introduced by numerical differentiation.

We close this section with the discussion of an algorithm similar to the polar expansion algorithm. This technique has not been used by the authors, but it has been used successfully by DeRosier and Klug and their colleagues [3], [14], [26], [27] to reconstruct from electron micrographs.

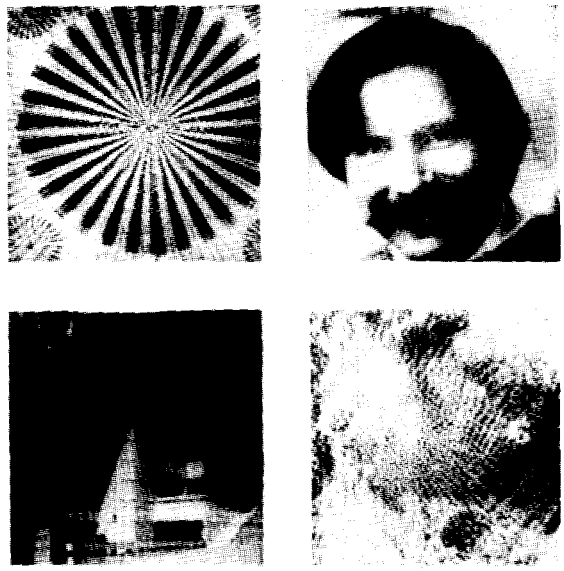

Fig. 10. Reconstruction of the pictures of Fig. 7 from 64 projections using the smearing algorithm.

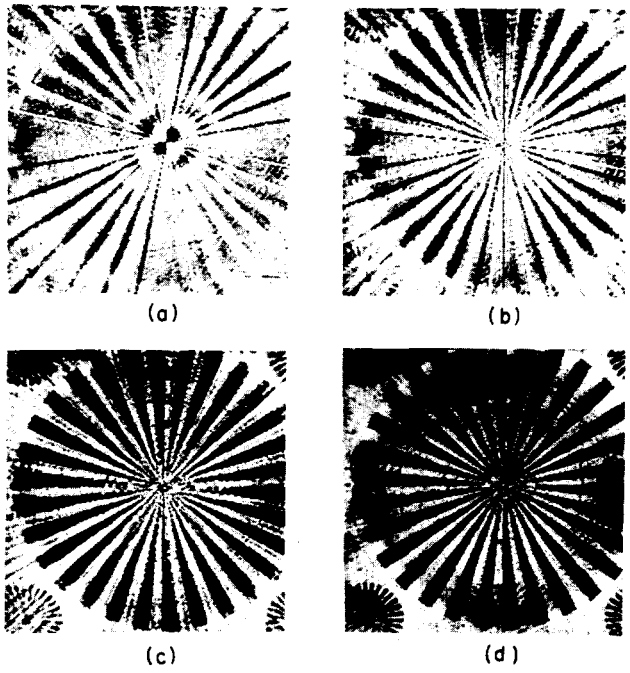

Fig. 11. Reconstruction of the test pattern of Fig. 7 using the smearing algorithm for different numbers of projections. (a) 16 projections. (b) 32 projections. (c) 64 projections. (d) 128 projections.

Let $f(r, \phi)$ represent the picture function in polar coordinates and let $F(\omega, \theta)$ represent its Fourier transform. Then, since $f(r, \phi)$ is necessarily a periodic function in ϕ with period 2π, we can express $f(r, \phi)$ in a Fourier series as

$$f(r, \phi) = \sum_{n=-\infty}^{\infty} f_n(r) \exp [jn\phi] \tag{58}$$

where

$$f_n(r) = \frac{1}{2\pi} \int_{-\pi}^{\pi} f(r, \phi) \exp [-jn\phi] \, d\phi. \tag{59}$$

However, since $f(r, \phi)$ and $F(\omega, \theta)$ are a Fourier transform pair it is true that

$$f(r, \phi) = \frac{1}{4\pi^2} \int_0^{\infty} \int_{-\pi}^{\pi} F(\omega, \theta) \exp [jr\omega \cos (\theta - \phi)] \, \omega \, d\theta d\omega. \tag{60}$$

Thus

$$f_n(r) = \frac{1}{2\pi} \int_{-\pi}^{\pi} \left\{ \frac{1}{4\pi^2} \int_0^{\infty} \int_{-\pi}^{\pi} F(\omega, \theta) \cdot \exp [jr\omega \cos (\theta - \phi)] \, \omega \, d\theta d\omega \right\} \exp [-jn\phi] \, d\phi. \tag{61}$$

Interchanging the order of the integrations,

$$f_n(r) = \frac{1}{8\pi^3} \int_0^{\infty} \int_{-\pi}^{\pi} F(\omega, \theta) \, \omega \, d\theta d\omega \cdot \int_{-\pi}^{\pi} \exp [j(r\omega \cos (\phi - \theta) - n\phi)] \, d\phi \tag{62}$$

$$= \frac{1}{8\pi^3} \int_0^{\infty} \int_{-\pi}^{\pi} F(\omega, \theta) \exp \left[jn \left(\theta + \frac{\pi}{2} \right) \right] \omega \, d\theta d\omega \cdot \int_{-\pi+\theta}^{\pi+\theta} \exp [jr\omega \sin \alpha - n\alpha] \, d\alpha \tag{63}$$

$$= \frac{1}{4\pi^2} \int_0^{\infty} \int_{-\pi}^{\pi} F(\omega, \theta) \exp \left[jn \left(\theta + \frac{\pi}{2} \right) \right] J_n(r\omega) \, d\theta d\omega \tag{64}$$

where $J_n(x)$ is the nth-order Bessel function of the first kind. Since $F(\omega, \theta)$ is a periodic function in θ with period 2π we can express it in a Fourier series as well, as

$$F(\omega, \theta) = \sum_{n=-\infty}^{\infty} F_n(\omega) \exp \left[+jn \left(\theta + \frac{\pi}{2} \right) \right] d\theta. \tag{65}$$

The factor of $\pi/2$ has been included in the exponent of (65) so that by comparing (65) and (64) we can see that

$$f_n(r) = \frac{1}{2\pi} \int_0^{\infty} F_n(\omega) \, J_n(r\omega) \, d\omega \tag{66}$$

$$F_n(\omega) = \int_0^{\infty} f_n(r) \, J_n(r\omega) \, dr. \tag{67}$$

(66) and (67) say that $f_n(r)$ and $F_n(\omega)$ form a Fourier-Bessel or Hankel transform pair.

From this derivation we can formulate a reconstruction algorithm. From the slices we compute the sequences $F_n(\omega)$ using the inverse of (65). If the slice angles are evenly spaced, this can be done using a DFT. Then we can take the nth-order Hankel transform of each of the $F_n(\omega)$ to obtain the $f_n(r)$. Then, using another DFT calculation, $f(r, \phi)$ can be approximated on any desired number of radii and angles.

The major difficulties with this technique are computational. Each of the Hankel transforms which must be taken is different since each uses a different Bessel function. The amount of computation can, therefore, be large. DeRosier and Klug [3], in their original work, reconstructed helices. The unique properties of helices allowed them to obtain several of the $F_n(\omega)$ from a single projection.

V. Approximate Reconstruction from a Concentric-Squares Raster

In Section III we considered a procedure for exact reconstruction of a band-limited function of finite order based on using the projections to obtain samples of the Fourier transform on a concentric-squares raster. An exact reconstruction procedure then consists of interpolating or extrapolating from this concentric-squares raster to a Cartesian raster. Since the vertical lines of the concentric-squares and Cartesian rasters are identical, interpolation from a concentric-squares raster to a Cartesian raster involves only one-dimensional interpolation rather than two-dimensional interpolation as was required for the polar raster.

One difficulty with the concentric-squares raster is that with the slices confined to the range $-(\pi/4) \leqslant \theta \leqslant +(\pi/4)$, as was done in Section III, for small radial values the samples are closely spaced over a small frequency range and consequently extrapolation far away from these points is necessary.

In this section we consider a modification of this procedure. In particular, by generalizing the raster of Fig. 2 to include additional projections, it is possible to avoid the extrapolation problem previously mentioned. In addition, for approximate reconstruction, we will use low-order interpolation.

In deriving the polar raster it was assumed that the Fourier transform of the unknown was confined to a circular region in the Fourier plane of radius $\sqrt{2}\, W$. Here we assume that it is instead confined to a square region of half-side W, as illustrated in Fig. 12. It should be noted that such a function is also confined to a disk of radius $\sqrt{2}\, W$.

For such a function, by the projection-slice theorem it is seen that each projection can be represented by a band-limited function whose bandwidth is a function of the projection angle θ. Thus we can represent the projection at angle θ, $p_\theta(u)$ by

$$p_\theta(u) = \sum_{n=-\infty}^{\infty} p_\theta \left(\frac{n\pi}{W_\theta} \right) \frac{\sin W_\theta \left(u - \frac{n\pi}{W_\theta} \right)}{W_\theta \left(u - \frac{n\pi}{W_\theta} \right)} \tag{68}$$

where

$$W_\theta \geqslant \frac{W}{\max \{|\cos \theta|, |\sin \theta|\}}. \tag{69}$$

The right-hand side of (69) specifies the minimum sampling rate that can be used to sample the projection of a band-limited function of angle θ. If a lower sampling rate is used, information will be lost through the sampling process. If each projection is sampled at this rate and the resulting sequences are transformed by using an N point DFT to compute the sum

$$S_\theta(k\Delta\omega) = \sum_{n=-\infty}^{\infty} p_\theta \left(\frac{n\pi}{W_\theta} \right) \exp \left[-j \frac{2\pi}{N} nk \right], \qquad k = -\frac{N}{2} + 1, \cdots, 0, \cdots, \frac{N}{2}$$

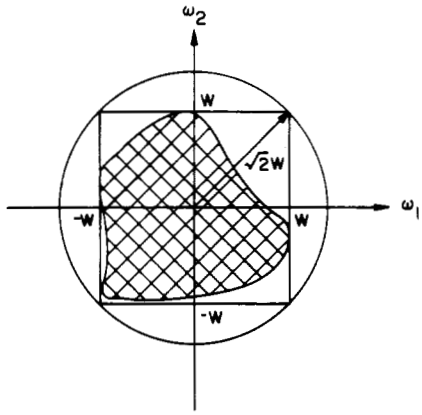

Fig. 12. Illustration of the Fourier transform confined to a square region of half side W.

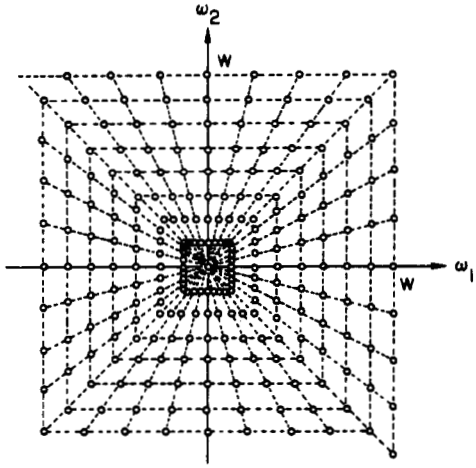

Fig. 13. A concentric-squares raster.

we will obtain a set of slice samples that are different from the polar case. In fact, we can in general control where the samples of $S_\theta(\omega)$ are located by controlling the sampling interval used to sample the projection $p_\theta(u)$. We shall define a concentric-square raster to be a raster of sample locations formed by sampling a finite number of projections at their respective Nyquist rates and then taking N point transforms of the results. Such a raster is illustrated in Fig. 13.

As a comment, it should be noted that if the projections are made by a source of collimated radiation such as an X-ray source then concentric-squares samples can be obtained with a hardware scanner which does not have an adjustable sampling interval. This technique is illustrated in Fig. 14. Assume that the object that we wish to identify is irradiated by a collimated beam and that it lies between the beam source and a recording surface such as a photographic plate. Instead of rotating the unknown to produce different projections, the beam and the photographic plate will be moved simultaneously. In particular, assume that we begin with the beam perpendicular to the x axis and the plate parallel to the x axis as indicated in Fig. 14(a). As the beam is rotated, the center of the plate is shifted as indicated in Fig. 14(b). When the projection angle exceeds $\pi/4$, the plate is placed parallel to the y axis as indicated in Fig. 14(c), and as the projection angle increases further, the center of the plate shifts accordingly, as indicated in Fig. 14(d). Thus the photographic plate is moved in such a way that its center follows a square. In this way the

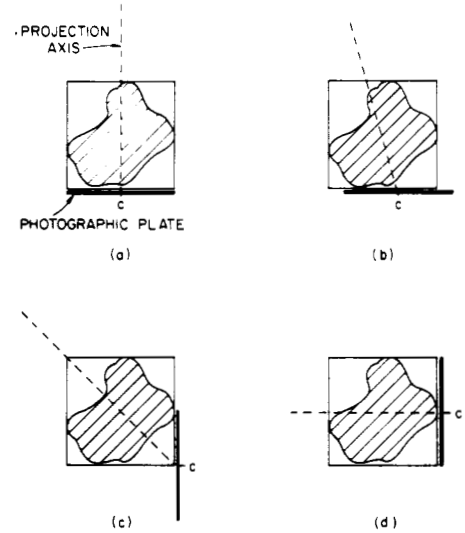

Fig. 14. Illustration of a technique for obtaining projections for concentric-squares samples.

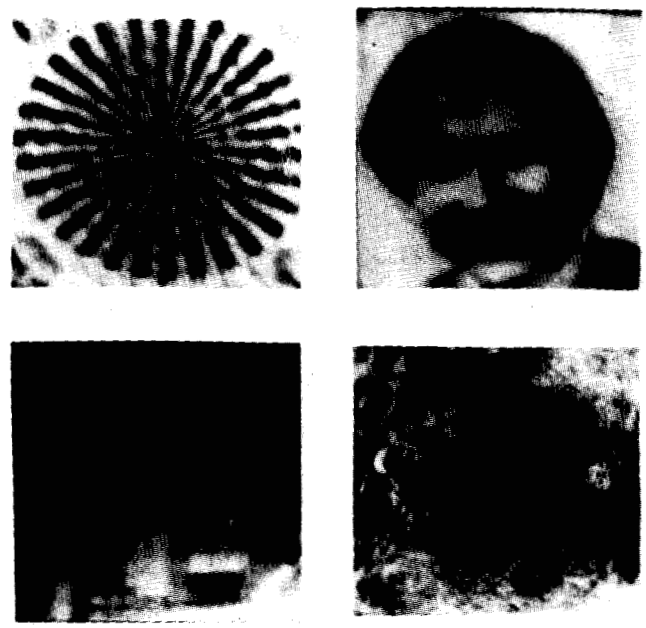

Fig. 15. Reconstructions of the pictures of Fig. 7 using linear interpolation from a concentric-squares raster of 64 evenly spaced slices.

recorded picture is seen to be expanded by a factor of

$$\frac{1}{\max\{|\cos\theta|, |\sin\theta|\}}$$

by the obliqueness of the recording surface. If all projections are now sampled with the same sampling interval, π/W, the resulting sequences correspond to a set of sampled projections on a concentric-squares raster.

As with the polar raster, we can use linear interpolation to estimate the values of Cartesian samples of $F(\omega_1, \omega_2)$ from the known samples on the concentric-squares raster.

Fig. 15 shows some reconstructions made by using linear interpolation from a concentric-squares raster of 64 evenly spaced slices. In Fig. 16 we have used a similar algorithm with a different set of slice (projection) angles. Instead of choosing the angles to be evenly spaced, we have chosen them

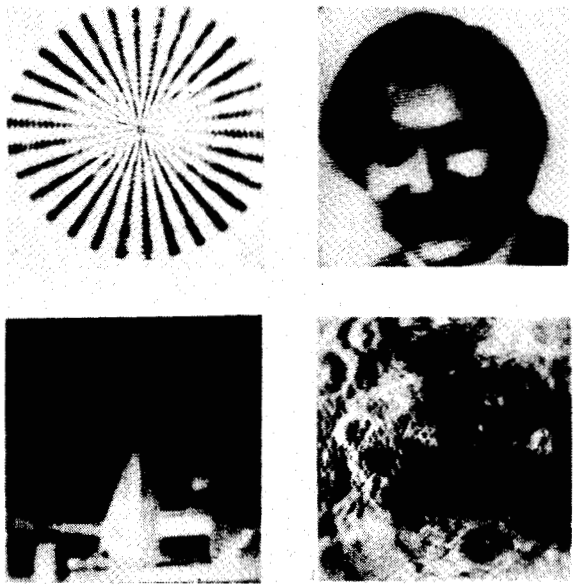

Fig. 16. Reconstruction of the pictures of Fig. 7 using the same algorithm as for Fig. 15 but with a different set of projection angles.

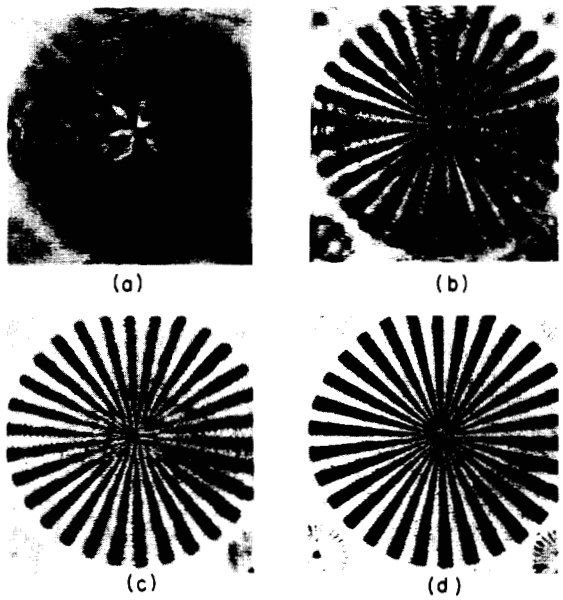

Fig. 17. Reconstruction of the test pattern of Fig. 7 using the identical algorithm as for Fig. 16 but varying the number of projections. (a) 16 projections. (b) 32 projections. (c) 64 projections. (d) 128 projections.

so that the intersections of the slices with the concentric squares are evenly spaced on each square. This set of angles yields a computationally simpler algorithm and it results in a higher density of samples in the "corners" of the nonzero region of $F(\omega_1, \omega_2)$. It should be noted that these two different sets of projection angles yield virtually identical reconstructions. In Fig. 17 we have taken this latter strategy for choosing projection angles and examined reconstructions made with 16, 32, 64, and 128 projections to see what improvement in reconstruction quality could be gained by adding more projections.

From these examples we note that the reconstructions from linear interpolation from a concentric-squares raster seem to be of better quality than those from a polar raster. This is probably due to two factors. The interpolation is one-dimensional and the Fourier transforms of the photographs used have regions of support in the Fourier plane which are more nearly square than circular. From Fig. 17 we note a steady improvement in reconstruction quality with increased projections. This result is certainly not surprising. The improvement is particularly striking when we go from 32 to 64 projections, although this is somewhat dependent upon the example chosen which has 30 circularly arranged black spokes.

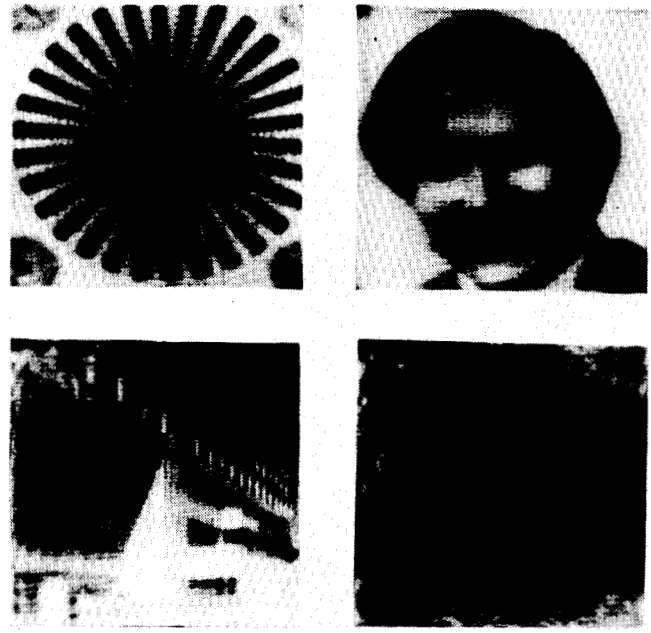

Fig. 18. Reconstruction based on high-order polynomial interpolation along the sides of a series of concentric squares.

As the preceding algorithm represented a straightforward extension of the polar linear interpolation algorithm, so also can we extend the polar expansion algorithm and compute extra concentric-squares slices from a limited number which are available from projections. Instead of performing an expansion in polar coordinates, however, we must perform it in "concentric-squares coordinates," i.e., along the slice lines and along the squares. Actual interpolation along the slices is unnecessary since all of the concentric-squares samples already lie on the squares which contain all of the DFT samples—this, of course, is the advantage of using concentric-squares coordinates. Thus our algorithm reduces to the implementation of a high-order polynomial interpolation (in $\exp[j\omega_1]$ or $\exp[j\omega_2]$) along the sides of a series of concentric squares, a task that can be accomplished using a DFT.

Suppose, for example, that N_v slices intersect the vertical sides of an array of concentric squares where $N_v \geq N$. (If $N_v \leq N$, then by the arguments of Section III, exact reconstruction can be performed.) We can approximate $F(\omega_1, \omega_2)$ along each vertical side by a polynomial of degree $N_v - 1$ in the variable $\exp[-j(\pi/W)\omega_2]$. Similarly, if each horizontal side is intersected by N_h slices ($N_h < N$), we can approximate $F(\omega_1, \omega_2)$ along these lines by a polynomial of degree $N_h - 1$ in the variable $\exp[j(\pi/W)\omega_1]$. We know, however, that $f(x_1, x_2)$ is of finite order and that in fact $F(\omega_1, \omega_2)$ varies as a polynomial of degree $N - 1$ in the appropriate variable along all of these lines. Thus to the extent that the higher order polynomial can be closely approximated by the lower one, we can expect an accurate reconstruction.

Fig. 18 illustrates four reconstructions performed by this technique. Whereas these reconstructions represent an im-

provement over the corresponding polar reconstructions, they represent very little improvement over the straightforward linear interpolation from a concentric-squares raster.

As a final step in our development of parallel polar and concentric-squares reconstruction algorithms, it remains to implement the smearing algorithm in concentric-squares fashion. This is straightforward. First, we must express $F(\omega_1, \omega_2)$ in concentric-squares coordinates. Defining ω to be a variable that designates the square of interest, i.e., ω remains constant on each square, and λ as the normalized arc length, we obtain

$$\begin{aligned} f(x_1, x_2) &= \frac{1}{4\pi^2} \int_0^W \int_0^1 \omega \hat{F}(\omega, \lambda) \exp\left[j\omega(x_1 + \lambda x_2)\right] d\lambda d\omega \\ &- \frac{1}{4\pi^2} \int_0^W \int_1^3 \omega \hat{F}(\omega, \lambda) \exp\left[j\omega((2-\lambda)x_1 + x_2)\right] d\lambda d\omega \\ &- \frac{1}{4\pi^2} \int_0^W \int_3^5 \omega \hat{F}(\omega, \lambda) \exp\left[j\omega(-x_1 + (4-\lambda)x_2)\right] d\lambda d\omega \\ &+ \frac{1}{4\pi^2} \int_0^W \int_5^7 \omega \hat{F}(\omega, \lambda) \exp\left[j\omega((\lambda-6)x_1 - x_2)\right] d\lambda d\omega \\ &+ \frac{1}{4\pi^2} \int_0^W \int_7^8 \omega \hat{F}(\omega, \lambda) \exp\left[j\omega(x_1 + (\lambda-8)x_2)\right] d\lambda d\omega. \end{aligned} \tag{70}$$

Now we can apply the trapezoidal rule to the samples in concentric-squares coordinates. We shall assume that the samples are located on a regular concentric-squares raster, i.e., evenly spaced in ω and evenly spaced in λ. We thus obtain a summation that very much resembles the similar result in polar coordinates:

$$\begin{aligned} f(x_1, x_2) &= \frac{4W^2}{8M^2\pi^2} S_{\theta_0}(0) \\ &+ \frac{4W^2}{NM^2\pi^2} \sum_{i=0}^{N/4-1} \sum_{k=-M/2+1}^{M/2} |k| \hat{F}\left(\frac{2Wk}{M}, \frac{4i}{N}\right) \\ &\cdot \exp\left[j \frac{2Wk}{M}\left(x_1 - \frac{4i}{N} x_2\right)\right] \\ &+ \frac{4W^2}{NM^2\pi^2} \sum_{i=N/4}^{3N/4-1} \sum_{k=-M/2+1}^{M/2} |k| \hat{F}\left(\frac{2Wk}{M}, \frac{4i}{N}\right) \\ &\cdot \exp\left[j \frac{2Wk}{M} \frac{2N-4i}{N} (x_1 + x_2)\right] \\ &+ \frac{4W^2}{NM^2\pi^2} \sum_{i=3N/4}^{N-1} \sum_{k=-M/2+1}^{M/2} |k| \hat{F}\left(\frac{2Wk}{M}, \frac{4i}{N}\right) \\ &\cdot \exp\left[j \frac{2Wk}{M}\left(-x_1 + \frac{4N-4i}{N} x_2\right)\right]. \end{aligned} \tag{71}$$

Equation (71) can be shown to have an interpretation in terms of smearing exactly as in the polar case. Each projection is sampled, and transformed to obtain concentric-squares samples of $F(\omega_1, \omega_2)$. They are then multiplied by the weighting function $|\omega|$, inverse-transformed, and back-projected as before. As in the polar case, the mean gray levels of the original and of the reconstruction are adjusted to be equal.

Fig. 19. Reconstructions obtained by using concentric-squares smearing.

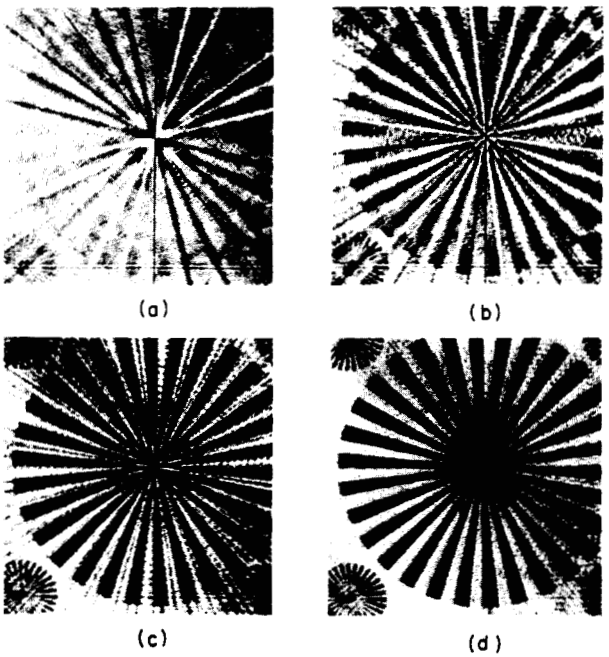

Fig. 20. Reconstruction of the test pattern of Fig. 7 using concentric-squares smearing for several choices of the number of projections. (a) 16 projections. (b) 32 projections. (c) 64 projections. (d) 128 projections.

Fig. 19 presents some reconstructions generated by using concentric-squares smearing and in Fig. 20 we present some reconstructions of one of these photographs for 16, 32, 64, and 128 projections. It should be noted that the quality of the reconstructions, at least when more than 64 projections are used, is very good—in fact, it is better than with any other algorithm used for this paper.

One objection to the use of the concentric-squares raster might be that it assumes a particular orientation for the object being reconstructed and that the projections are not all being treated equally in some sense. There are two important cases, however, in which this can be a distinct advantage. One is

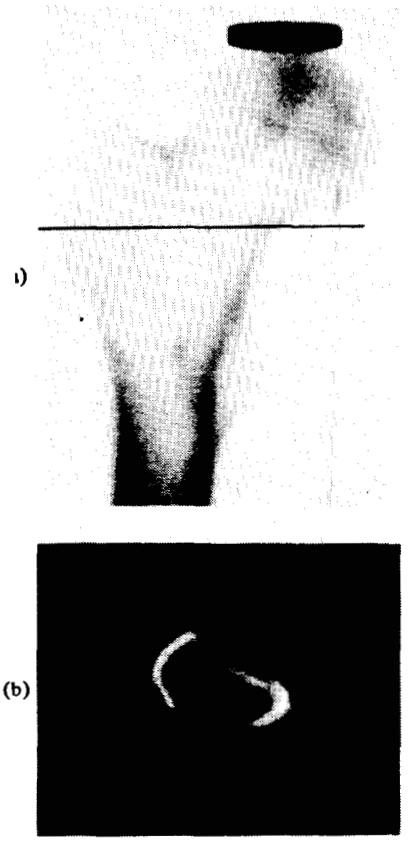

Fig. 21. Reconstruction from a series of X-rays of an excised human femur using the concentric-squares linear interpolation algorithm. (a) One of the set of X-rays. (b) Reconstruction of cross section at the level of the dark line indicated in Fig. 21(a).

when the unknown itself has a preferred orientation, i.e., when it tends to have a square region of support. The second is when the reconstruction algorithm itself does not treat all projections identically. This class of algorithms includes all of the interpolation algorithms which perform an inverse two-dimensional DFT, but does not include the smearing algorithm or the algorithm in Section IV which uses Hankel transforms.

In an effort to see how well one of these algorithms would perform on real data, a series of X-rays of an excised human femur were obtained. The complete series consisted of 36 X-rays which were taken normal to the long axis of the bone at 5° intervals. Since the algorithms were all designed to perform two-dimensional reconstructions from one-dimensional projections, each of the X-rays was sampled logarithmically along a single line normal to the long axis and a single cross section of the bone was reconstructed. Each projection was sampled at 256 points and the sampling interval was the same for each projection. These samples were then used to compute both polar and concentric-squares samples of $F(\omega_1, \omega_2)$. The concentric-squares linear interpolation reconstruction is presented in Fig. 21(b) and one of the X-rays from which it is produced is in Fig. 21(a). The hollow tubular structure of the bone is evident from this reconstruction. In addition, material of lighter density is seen inside the bone. The reconstruction from a polar grid was virtually identical.

VI. Algebraic Reconstruction Techniques

In the previous sections we have concentrated on a number of reconstruction algorithms that are conveniently interpreted in Fourier space. In this section we wish to briefly discuss a

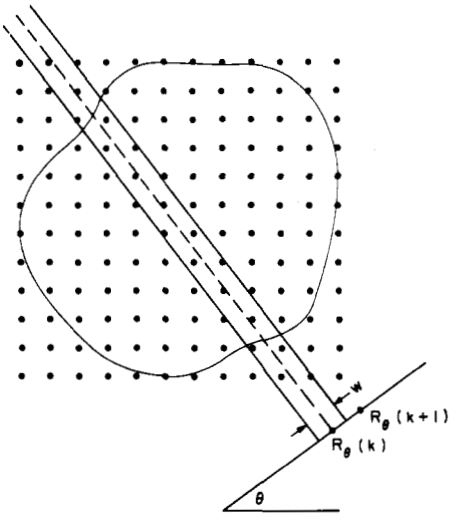

Fig. 22. Procedure for obtaining the kth value of the pseudo-projection at angle θ.

class of algebraic reconstruction techniques which are implemented directly in signal space. A variety of such approaches have been proposed by Gordon, Bender, and Herman [9]; Gilbert [10]; Goitein [28]; and Hounsfield [11]. The latter has resulted in a marketable device for performing brain scans. All of these techniques begin with the assumption that the object to be reconstructed is a sampled array, i.e., it is represented by samples of its density on a Cartesian grid. A pseudo-projection at angle θ for such an object is defined by considering the sum of the densities contained within a set of rays of width w parallel to the projection axis. For a two-dimensional object, for example, we consider the object as representable by the densities $\rho(i, j)$ on a Cartesian grid. The kth value of pseudo-projection at angle θ, denoted by $R_\theta(k)$, is obtained as indicated in Fig. 22. Specifically, $R_\theta(k)$ is equal to the sum of the densities associated with the points contained within the indicated ray.

If the projections from which the object is to be reconstructed corresponded to the pseudo-projections, then, in principle, the reconstruction could be carried out algebraically. Specifically, if the unknown can be represented by an $N \times N$ grid then it is defined by N^2 density values. Each pseudo-projection value $R_\theta(k)$ represents a linear equation in the N^2 unknown density values. Thus with a sufficient number of projections a set of N^2 linear equations can be obtained which can then be solved for the unknown densities $\rho(i, j)$. For any reasonable value of N this would result in a large number of equations—too many equations in fact to solve algebraically in a practical system. As an additional consideration, the approximation of pseudo-projections by projections and the effect of measurement errors are likely to make the set of N^2 equations ill-conditioned or inconsistent. Therefore, the equations are solved approximately in an iterative fashion. This removes the constraint that the number of equations equal N^2. In fact, Hounsfield uses $4N^2$ equations and Gordon, Bender, and Herman use a much smaller number, typically $N^2/4$ or so.

In the class of algebraic reconstruction techniques, an initial set of densities for the object are assumed. These initial densities are then changed iteratively in such a manner that the calculated pseudo-projections converge to the available projection data. A variety of methods have been proposed for iteratively changing the densities and the reader is referred to

the literature for specific discussions of the various methods. A typical approach is the following adapted from Herman, Lent, and Rowland [29]. Let $P_\theta(k)$ denote samples of the projection at angle θ and $R_\theta^q(k)$ the pseudo-projection at angle θ on the qth iteration of the algorithm. Furthermore, let $\rho^q(i, j)$ denote the density at the i, jth point on the qth iteration. The algorithm then sets

$$\rho^{q+1}(i,j) = \rho^q(i,j) + \delta(i,j,k,\theta)\frac{R_\theta(k) - R_\theta^q(k)}{N_{\theta,k}} \quad (72)$$

where $\delta(i, j, k, \theta)$ is an indicator variable which is 1 when $\rho(i, j)$ is included in the ray corresponding to $R_\theta^q(k)$ and 0 when it is not and $N_{\theta,k}$ is the number of elements in that ray.

The family of algebraic reconstruction techniques has generated a certain amount of controversy [30], [31], which centers primarily on the comparison with Fourier methods. The development and modification of these techniques and the comparison with other methods appear to still be an active area of discussion. These techniques being signal space techniques have the important advantage that signal space constraints, such as the fact that densities are of necessity positive, are relatively easy to impose, whereas they suffer from the drawback that they become computationally inefficient for very large values of N. These techniques, like the Fourier space techniques, impose certain constraints upon the object to be reconstructed. Which set of constraints is the more appropriate will probably vary with the object under investigation and the required resolution of the finished reconstruction.

Acknowledgment

The authors were first introduced to this problem by Dr. B. Gold of the M.I.T. Lincoln Laboratories, who also suggested the possibility that it might benefit from digital signal processing techniques. They would like to express their appreciation for this suggestion and for his continuing interest. The authors would also like to thank Dr. O. Tretiak for providing the X-ray data used in the reconstruction of Fig. 21, and the Cognitive Information Processing Group in the M.I.T. Research Laboratory of Electronics for the use of their facilities for A/D and D/A conversion of the photographs.

References

[1] R. N. Bracewell, "Strip integration in radio astronomy," *Aust. J. Phys.*, vol. 9, pp. 198–217, 1956.
[2] R. N. Bracewell and A. C. Riddle, "Inversion of fan-beam scans in radio astronomy," *The Astrophys. J.*, vol. 150, pp. 427–434, 1967.
[3] D. J. DeRosier and A. Klug, "Reconstruction of three-dimensional structures from electron micrographs," *Nature*, vol. 217, pp. 130–134, 1968.
[4] B. K. Vainshtein, "Finding the structure of objects from projections," *Sov. Phys.—Crystall.*, vol. 15, no. 5, pp. 781–787.
[5] G. N. Ramachandran and A. V. Lakshminarayanan, "Three-dimensional reconstruction from radiographs and electron micrographs: II. Application of convolutions instead of Fourier transforms," *Proc. Nat. Acad. Sci.*, vol. 68, no. 9, pp. 2236–2240.
[6] J. B. Garrison, D. G. Grant, W. H. Guier, and R. J. Johns, "Three-dimensional roentgenography," *Amer. J. Roentgenol., Rad. Therapy, Nucl. Med.*, vol. 60, no. 4, pp. 903–908, 1969.
[7] O. Tretiak, D. Ozonoff, J. Klopping, and M. Eden, "Calculation of internal structure from multiple radiograms," in *Proc. Two-Dimensional Digital Signal Processing Conf.* (Univ. of Missouri-Columbia), pp. 6-2-1–6-2-3.
[8] G. T. Herman, "Two direct methods for reconstructing pictures from their projections: A comparative study," *Comp. Graph. Image Proc.*, vol. 1, pp. 123–144, 1973.
[9] R. Gordon, R. Bender, and G. T. Herman, "Algebraic reconstruction techniques (ART) for three-dimensional electron microscopy and X-ray photography," *J. Theor. Biol.*, vol. 29, pp. 471–481, 1970.
[10] P. Gilbert, "Iterative methods for the three-dimensional reconstruction of an object from projections," *J. Theor. Biol.*, vol. 36, pp. 105–117.
[11] G. N. Hounsfield, "Method and apparatus for measuring X or γ-radiation absorption or transmission at plural angles and analyzing the data," U.S. Patent 3 778 614, Dec. 11, 1973.
[12] R. M. Mersereau, "The digital reconstruction of multi-dimensional signals from their projections," Sc.D. dissertation, M.I.T., Dept. of Elec. Eng., 1973.
[13] ——, "Recovering multi-dimensional signals from their projections," *Comp. Graph. Image Proc.*, vol. 1, no. 6, pp. 179–195, Oct. 1973.
[14] R. M. Mersereau and D. E. Dudgeon, "The representation of two-dimensional sequences as one-dimensional sequences," *IEEE Trans. Acoust., Speech, Signal Processing*, vol. ASSP-22, pp. 320–325, Oct. 1974.
[15] P. R. Smith, T. M. Peters, and R. H. T. Bates, "Image reconstruction from finite numbers of projections," *J. Phys. A: Math, Nucl. Gen.*, vol. 6, pp. 361–382, 1973.
[16] R. A. Crowther, D. J. DeRosier, and A. Klug, "The reconstruction of a three-dimensional structure from projections and its application to electron microscopy," *Proc. Roy. Soc. London, Ser. A*, vol. 317, pp. 319–340, 1970.
[17] O. Tretiak, M. Eden, and W. Simon, "Internal structure from X-ray images," presented at the Int. Conf. on Medicine Biology in Engineering, 1969.
[18] A. Klug and R. A. Crowther, "Three-dimensional image reconstruction from the viewpoint of information theory," *Nature*, vol. 238, pp. 435–440, Aug. 25, 1972.
[19] D. J. DeRosier and P. B. Moore, "Reconstruction of three-dimensional images from electron micrographs of structures with helical symmetry," *J. Mol. Biol.*, vol. 52, pp. 355–369, 1970.
[20] D. J. DeRosier, "Three-dimensional image reconstruction of helical structures," *Ber. Bensen-Gesellschaft*, vol. 74, no. 11, pp. 1127–1128, 1970.
[21] L. A. Shepp and B. F. Logan, "The Fourier reconstruction of a head section," *IEEE Trans. Nucl. Sci.*, vol. NS-21, pp. 21–43, June 1974.
[22] B. K. Vainshtein, "Synthesis of projecting functions," *Sov. Phys.—Dokl.*, vol. 16, no. 2, pp. 66–69.
[23] G. N. Ramachandran, "Reconstruction of substance from shadow: I. Mathematical theory with application to three-dimensional radiography and electron," *Proc. Indian Acad. Sci.*, vol. 74, pp. 14–24.
[24] P. F. C. Gilbert, "The reconstruction of a three-dimensional structure from projections and its application to electron microscopy: II. Direct methods," *Proc. Roy. Soc. London, Ser. B*, vol. 182, pp. 89–102.
[25] D. G. Grant, J. B. Garrison, and R. J. Johns, "Three-dimensional radiography," *APL Tech. Dig.*, pp. 10–15, Jan. 1970.
[26] R. A. Crowther, L. A. Amos, J. T. Finch, D. J. DeRosier, and A. Klug, "Three-dimensional reconstructions of spherical viruses by Fourier synthesis from electron micrographs," *Nature*, vol. 226, pp. 421–425, 1970.
[27] R. A. Crowther, "Three-dimensional reconstruction and the architecture of spherical viruses," *Endeavor*, vol. 30, pp. 124–129.
[28] M. Goitein, "Three-dimensional density reconstruction from a series of two-dimensional projections," *Nucl. Instrum. Methods*, vol. 101, pp. 509–518, 1972.
[29] G. T. Herman, A. Lent, and S. Rowland, "ART: Mathematics and applications (a report on the mathematical foundations and on the applicability to real data of the algebraic reconstruction techniques)," *J. Theor. Biol.*, vol. 32, pp. 1–32, 1971.
[30] R. A. Crowther and A. Klug, "Art and science or conditions for three-dimensional reconstruction from electron micrograph images," *J. Theor. Biol.*, vol. 32, pp. 199–203, 1971.
[31] S. H. Bellman, R. Bender, R. Gordon, and J. E. Rowe, "ART is science, being a defense of algebraic reconstruction techniques for three-dimensional electron microscopy," *J. Theor. Biol.*, vol. 32, pp. 205–216, 1971.

Additional Bibliography

Fourier Space Techniques

In addition to [2], [3], [7], [12], [13], [19], [20], [26], [27]:

[32] R. A. Crowther, "Procedures for three-dimensional reconstruction of spherical viruses by Fourier synthesis from electron micrographs," *Phil. Trans. Roy. Soc. London, Ser. B*, vol. 261, pp. 221–230, 1971.
[33] R. A. Crowther and L. Amos, "Three-dimensional image reconstructions of some small spherical viruses," in *Proc. Cold Spring Harbor Symp.*, vol. 36, pp. 489–494, 1971.
[34] ——, "Harmonic analysis of electron microscope images with rotational symmetry," *J. Mol. Biol.*, vol. 60, pp. 123–130, 1971.

[35] D. J. DeRosier, "The reconstruction of three-dimensional images from electron micrographs," *Contemp. Phys.*, vol. 12, no. 5, pp. 437-452.
[36] A. Klug, "III. Applications of image analysis techniques in electron microscopy: Optical diffraction and filtering and three-dimensional reconstructions from electron micrographs," *Phil. Trans. Roy. Soc. London, Ser. A*, vol. 261, pp. 173-179.
[37] J. A. Lake, "Reconstruction of three-dimensional structures from sectioned helices by deconvolution of partial data," *J. Mol. Biol.*, vol. 66, pp. 255-269, 1972.
[38] R. M. Mersereau, "The digital reconstruction of multi-dimensional signals from their projections," in *Proc. 10th Annu. Allerton Conf. on Circuit and System Theory* (Oct. 4-6, 1972), pp. 326-334.
[39] T. M. Peters, P. R. Smith, and R. D. Gibson, "Computer aided transverse body-section radiography," *Brit. J. Radiol.*, vol. 46, pp. 314-317, 1973.

Direct Signal Space Techniques

In addition to [1], [4], [5], [8], [21]-[24]:

[40] A. M. Cormack, "Representation of a function by its line integrals, with some radiological applications," *J. Appl. Phys.*, vol. 34, pp. 2722-2727, 1963.
[41] ——, "Representation of a function by its line integrals with some radiological applications—II," *J. Appl. Phys.*, vol. 35, pp. 2908-2913, 1964.
[42] ——, "Reconstruction of densities from their projections, with applications in radiological physics," *Phys. Med. Biol.*, vol. 18, pp. 195-207, 1973.
[43] A. M. Mikhailov and B. K. Vainshtein, "Electron microscope determination of the three-dimensional structure of the extended tail of the P6 bacteriophage," *Sov. Phys.—Crystall.*, vol. 16, pp. 428-436, 1971.
[44] G. Muehllehner and R. A. Wetzel, "Section imaging by computer calculation," *J. Nucl. Med.*, vol. 12, pp. 76-84, 1972.
[45] G. N. Ramachandran and A. V. Lakshminarayanan, "Three-dimensional reconstruction from radiographs and electron micrographs: III. Description and application of the convolution method," *Indian J. Pure Appl. Phys.*, vol. 9, pp. 997-1003, 1971.
[46] B. K. Vainshtein and A. M. Mikhailov, "Some properties of the synthesis of projecting functions," *Sov. Phys.—Crystall.*, vol. 17, pp. 217-222, 1972.
[47] B. K. Vainshtein and S. S. Orlov, "Theory of the recovery of functions from their projections," *Sov. Phys.—Crystall.*, vol. 17, pp. 213-216, 1972.

Iterative Techniques

In addition to [8]-[11], [21], [28]-[31]:

[48] R. Bender, S. H. Bellman, and R. Gordon, "ART and the ribosome: A preliminary report on the three-dimensional structure of individual ribosomes determined by an algebraic reconstruction technique," *J. Theor. Biol.*, vol. 29, pp. 483-487, 1970.
[49] G. Frieder and G. T. Herman, "Resolution in reconstructing objects from electron micrographs," *J. Theor. Biol.*, vol. 33, pp. 189-211, 1971.
[50] N. T. Gaarder and G. T. Herman, "Algorithms for reproducing objects from their X-rays," *Comp. Graph. Image Proc.*, vol. 1, pp. 97-106.
[51] R. Gordon and G. T. Herman, "Reconstruction of pictures from their projections," *Commun. Ass. Comput. Mach.*, vol. 14, no. 12, pp. 759-768, Dec. 1971.
[52] G. T. Herman and S. Rowland, "Resolution in art: An experimental investigation of the resolving power of an algebraic picture reconstruction technique," *J. Theor. Biol.*, vol. 33, pp. 213-223, 1971.
[53] G. N. Hounsfield, "A method of and apparatus for examination of a body by radiation such as X or gamma radiation," Patent Office, London, England, Patent Specification 1 283 915, 1972.
[54] S. Krishnan, S. S. Prabhu, and E. V. Krishnamurthy, "Probabilistic reinforcement algorithms for the reconstruction of pictures from their projections," *Int. J. Syst. Sci.*, vol. 4, pp. 661-670, 1973.

Other Reconstruction Techniques

In addition to [6], [25]:

[55] S. K. Chang, "The reconstruction of binary patterns from their projections," *Commun. Ass. Comput. Mach.*, vol. 14, no. 1, pp. 21-25, Jan. 1973.
[56] S. K. Chang and C. K. Chow, "The reconstruction of three-dimensional objects from two orthogonal projections and its applications to cardiac cineangiography," *IEEE Trans. Comput.*, vol. C-22, pp. 18-28, Jan. 1973.
[57] S. K. Chang and G. L. Shelton, "Two algorithms for multiple-view binary pattern reconstruction," *IEEE Trans. Syst., Man, Cybern.* (Corresp.), vol. SMC-1, pp. 90-94, Jan. 1971.
[58] D. G. Grant, "TOMOSYNTHESIS: A three-dimensional radiographic imaging technique," *IEEE Trans. Biomed. Eng.*, vol. BME-19, pp. 20-28, Jan. 1972.
[59] D. E. Kuhl and R. Q. Edwards, "Reorganizing data from transverse section scans of the brain using digital processing," *Radiology*, vol. 91, pp. 975-983, 1968.
[60] E. R. Miller, E. M. McCurry, and B. Hruska, "An infinite number of laminagrams from a finite number of radiographs," *Radiology*, vol. 98, pp. 249-255, 1971.
[61] S. S. Sandler, "Direct three-dimensional analysis of electron micrograph pictures," *Pattern Recogn.*, vol. 4, pp. 353-359, 1972.

Others

[62] M. V. Berry and D. F. Gibbs, "The interpretation of optical projections," *Proc. Roy. Soc. London, Ser. A*, vol. 314, pp. 143-152, 1970.
[63] R. P. Kruger, E. C. Mahen, A. J. Carlson, S. J. Dwyer, and G. S. Lodwick, "Image analysis of radiograms," in *21st SWIEECO Rec.*, pp. 147-151.
[64] D. Ludwig, "The Radon transform on Euclidean space," *Commun. Pure Appl. Math.*, vol. 19, pp. 49-81, 1966.
[65] A. Papoulis, *Systems and Transforms with Applications in Optics*. New York: McGraw-Hill, 1968.
[66] J. Radon, "Ueber die Bestimmung von Funktionen durch Ihre Interralwerte Laengs Gewisser Mannigfaltigkeiten" (On the determination of functions from their integrals along certain manifolds), *Berichte Saechsische Akad. Wissenschaft. (Leipzig), Math. Phys. Klass 69*, pp. 262-271.

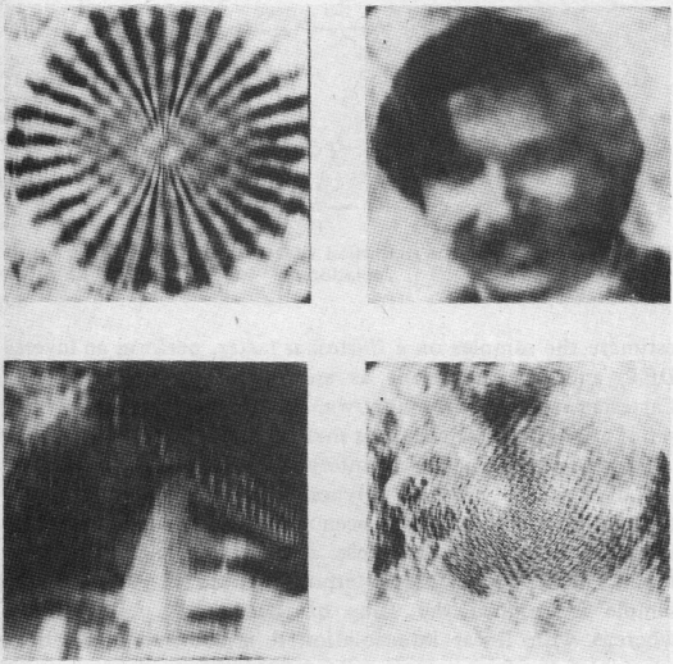

Fig. 5. Reconstruction of the pictures of Fig. 7 from their projections using zeroth-order interpolation from a polar raster.

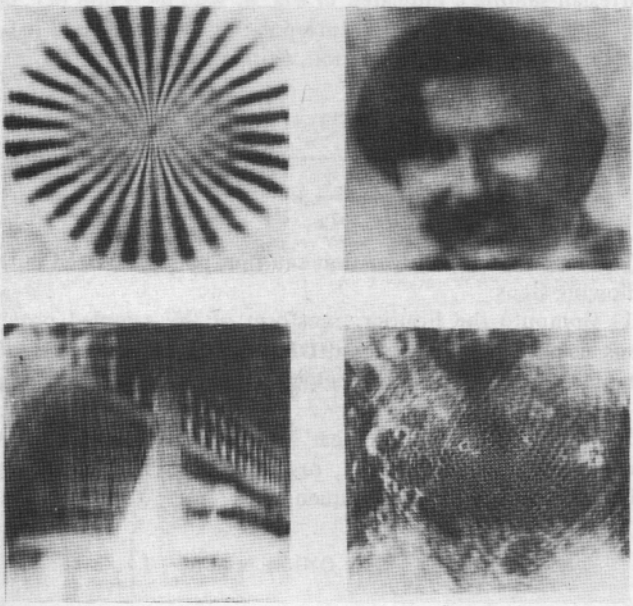

Fig. 6. Reconstruction of the pictures of Fig. 7 from their projections using linear interpolation from a polar raster.

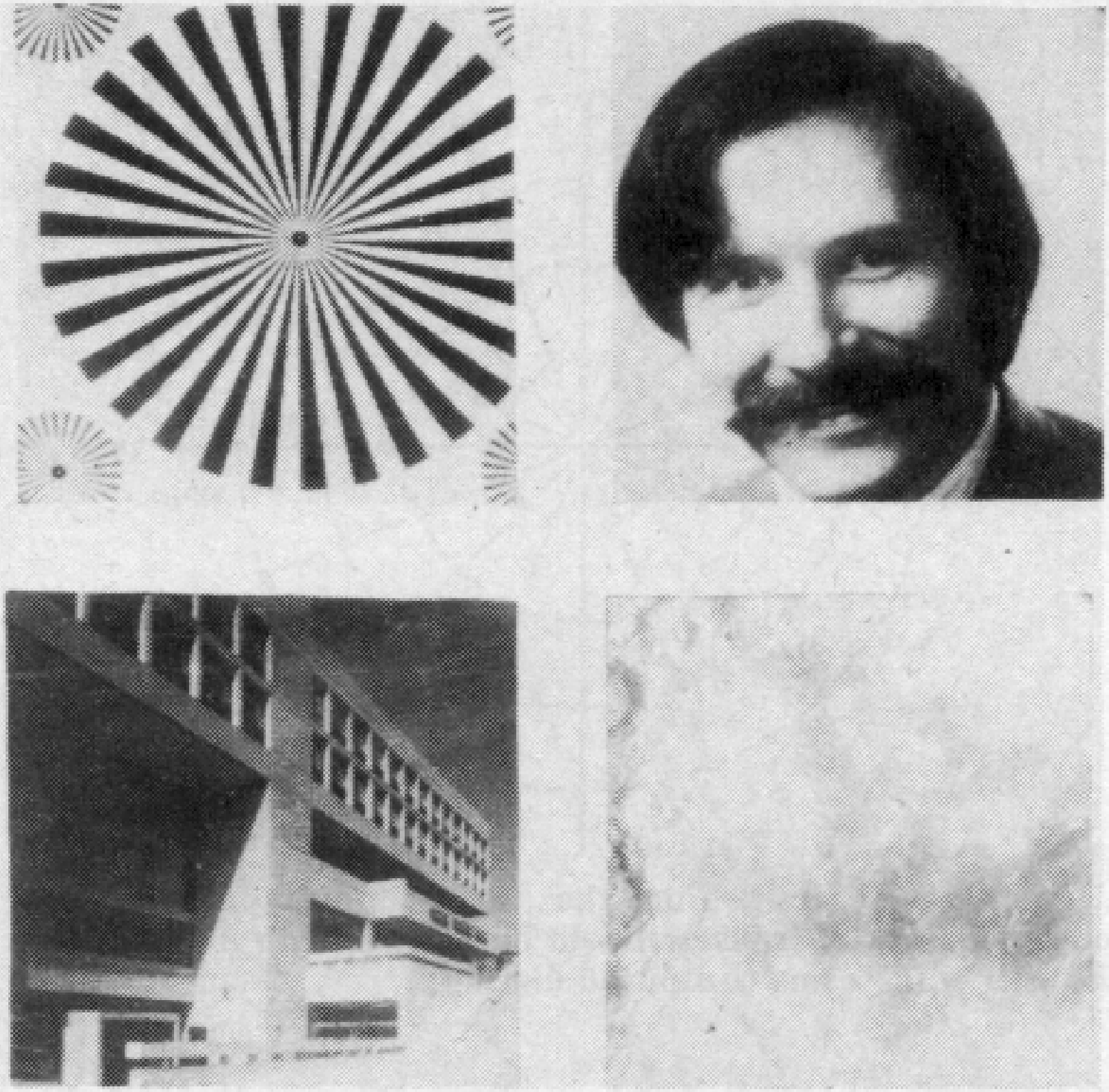

Fig. 7. Four original pictures for which the reconstruction from projections is to be carried out using a variety of algorithms.

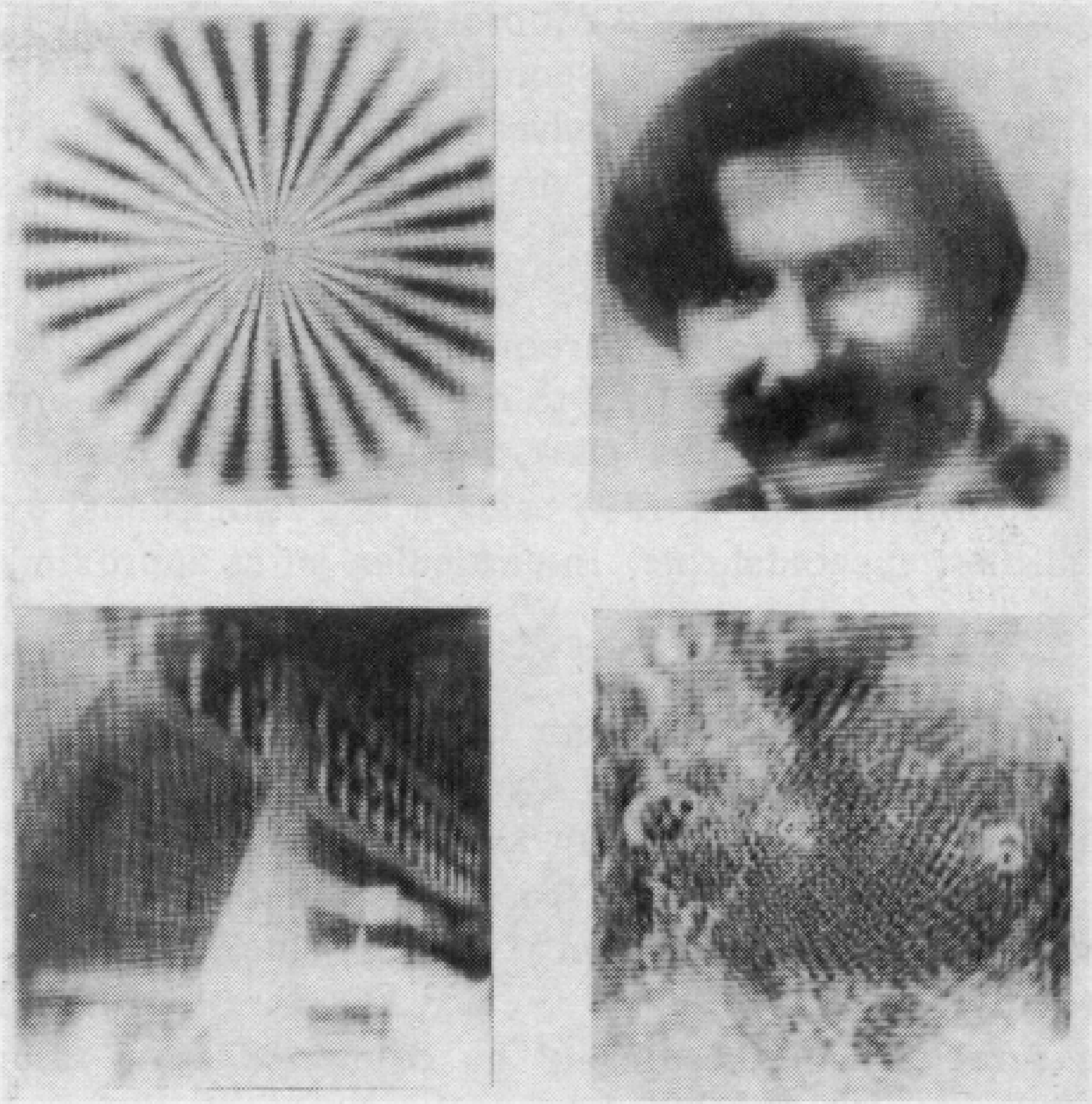

Fig. 8. Reconstruction of the pictures of Fig. 7 from their projections using the polar expansion algorithm.

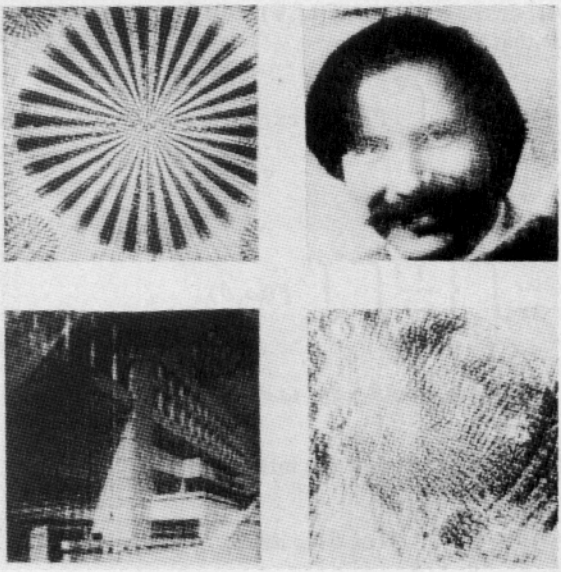

Fig. 10. Reconstruction of the pictures of Fig. 7 from 64 projections using the smearing algorithm.

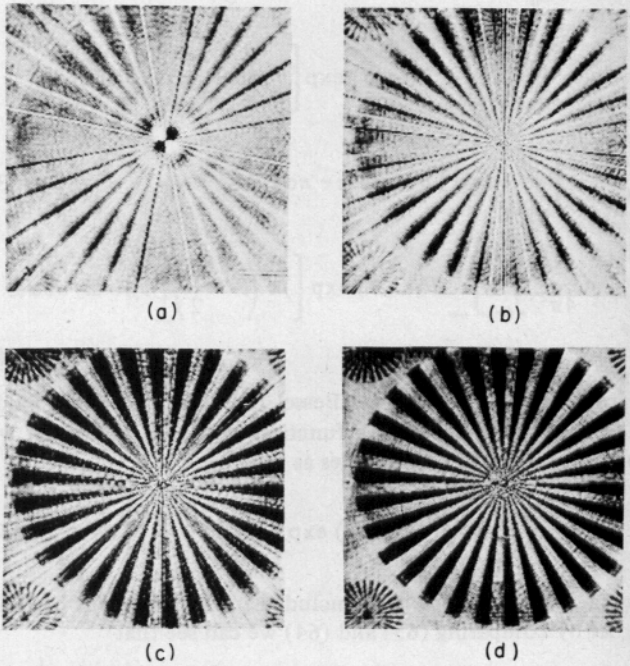

Fig. 11. Reconstruction of the test pattern of Fig. 7 using the smearing algorithm for different numbers of projections. (a) 16 projections. (b) 32 projections. (c) 64 projections. (d) 128 projections.

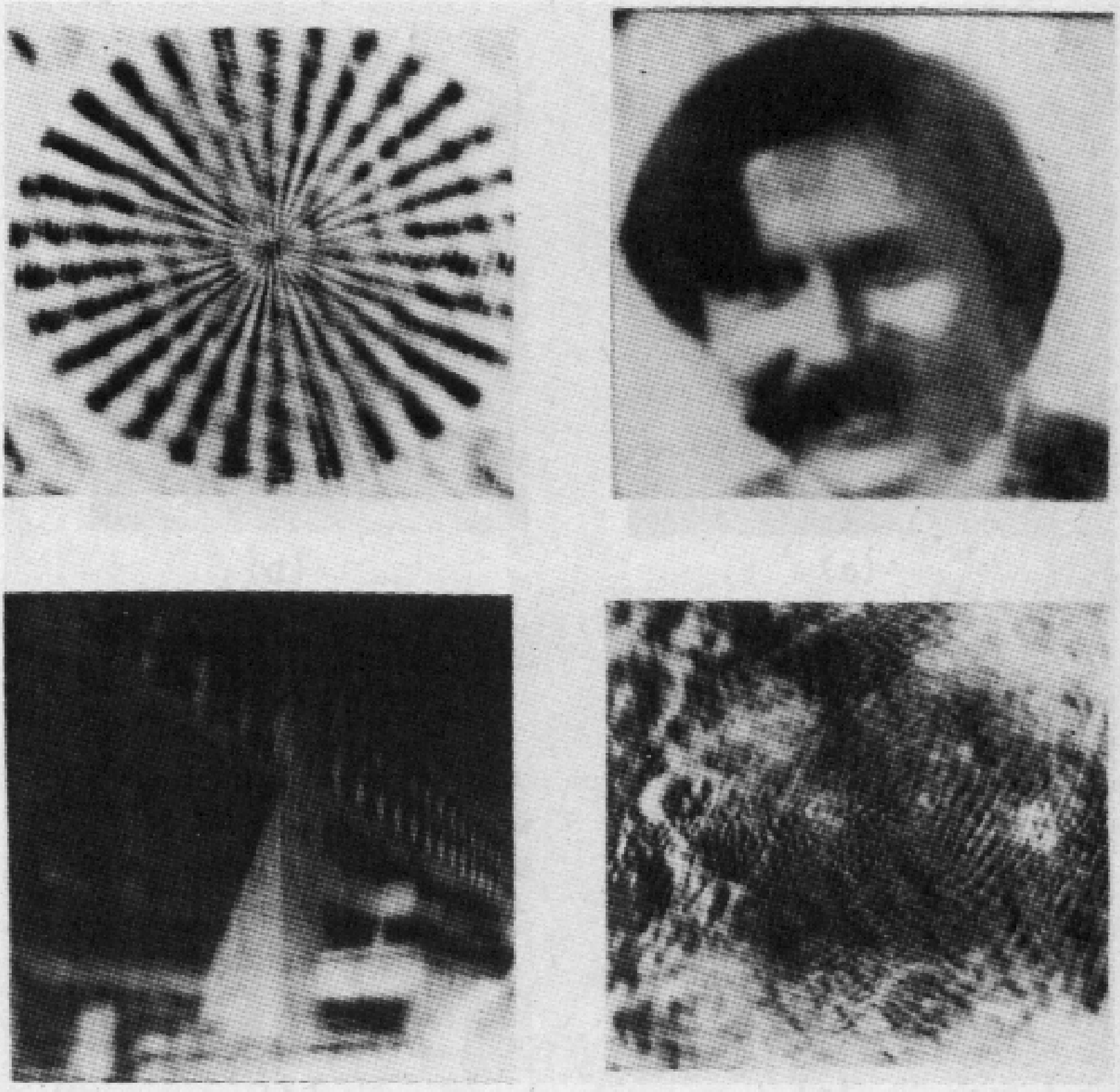

Fig. 15. Reconstructions of the pictures of Fig. 7 using linear interpolation from a concentric-squares raster of 64 evenly spaced slices.

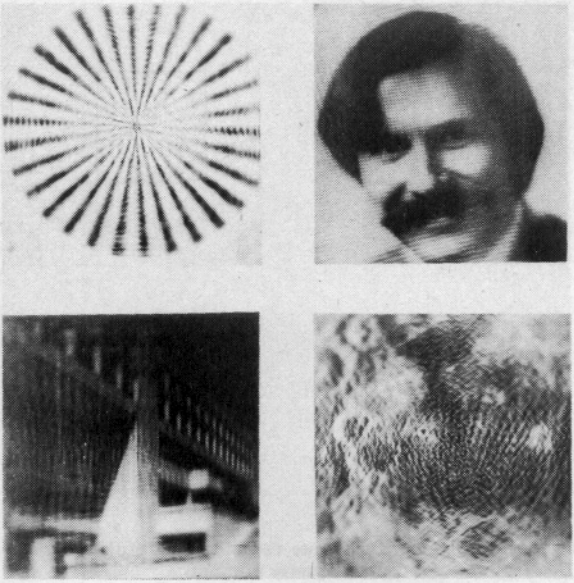

Fig. 16. Reconstruction of the pictures of Fig. 7 using the same algorithm as for Fig. 15 but with a different set of projection angles.

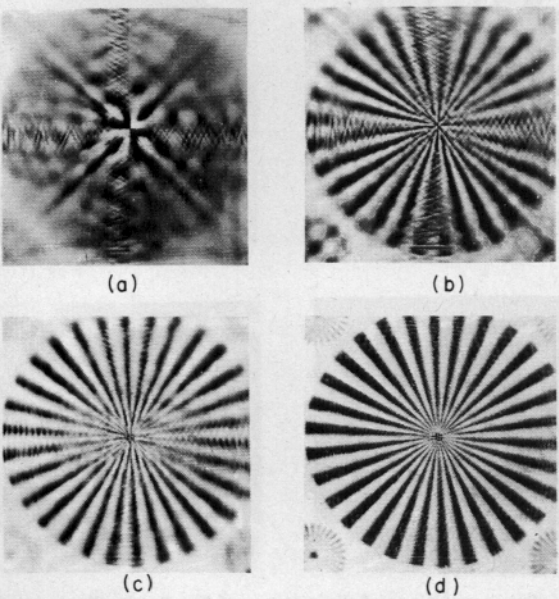

Fig. 17. Reconstruction of the test pattern of Fig. 7 using the identical algorithm as for Fig. 16 but varying the number of projections. (a) 16 projections. (b) 32 projections. (c) 64 projections. (d) 128 projections.

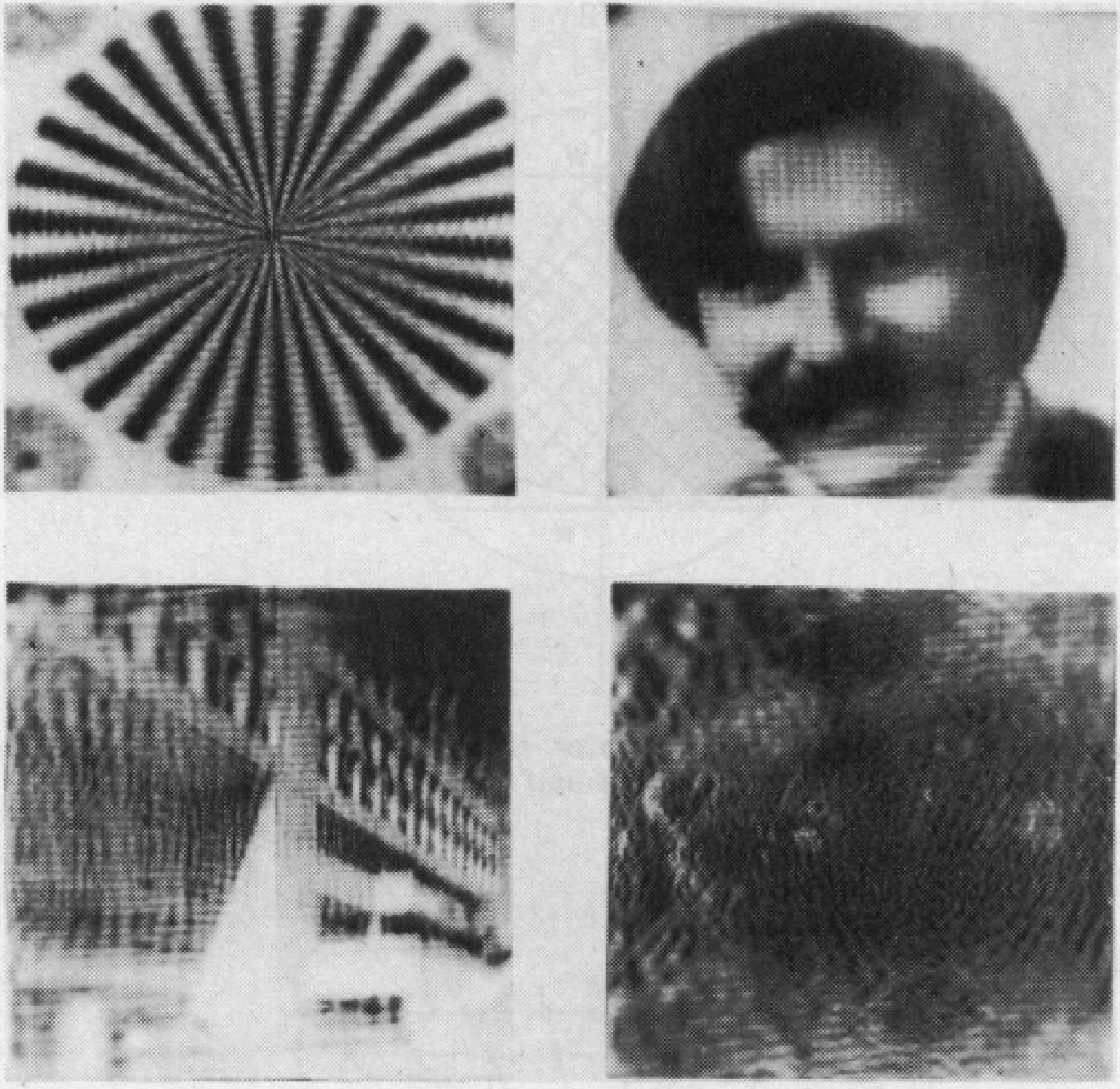

Fig. 18. Reconstruction based on high-order polynomial interpolation along the sides of a series of concentric squares.

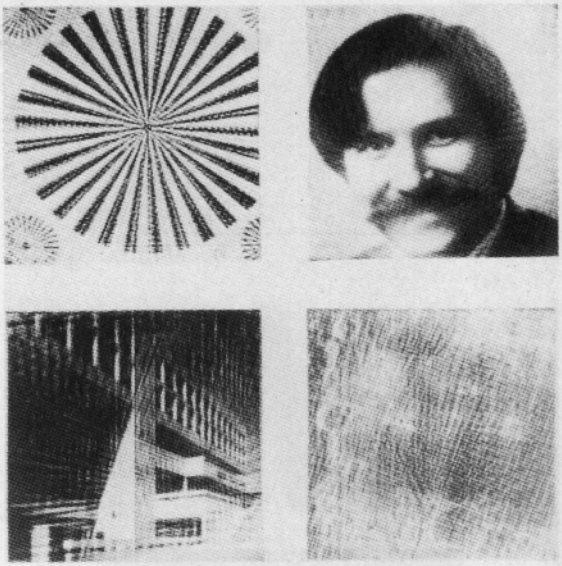

Fig. 19. Reconstructions obtained by using concentric-squares smearing.

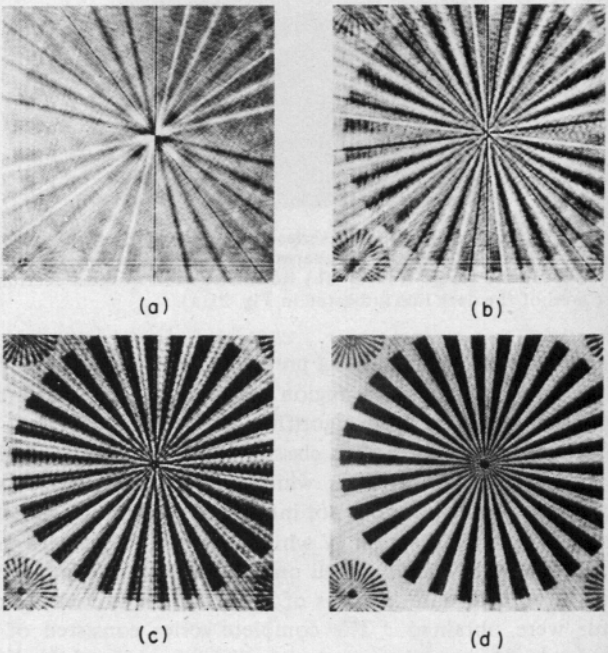

Fig. 20. Reconstruction of the test pattern of Fig. 7 using concentric-squares smearing for several choices of the number of projections. (a) 16 projections. (b) 32 projections. (c) 64 projections. (d) 128 projections.

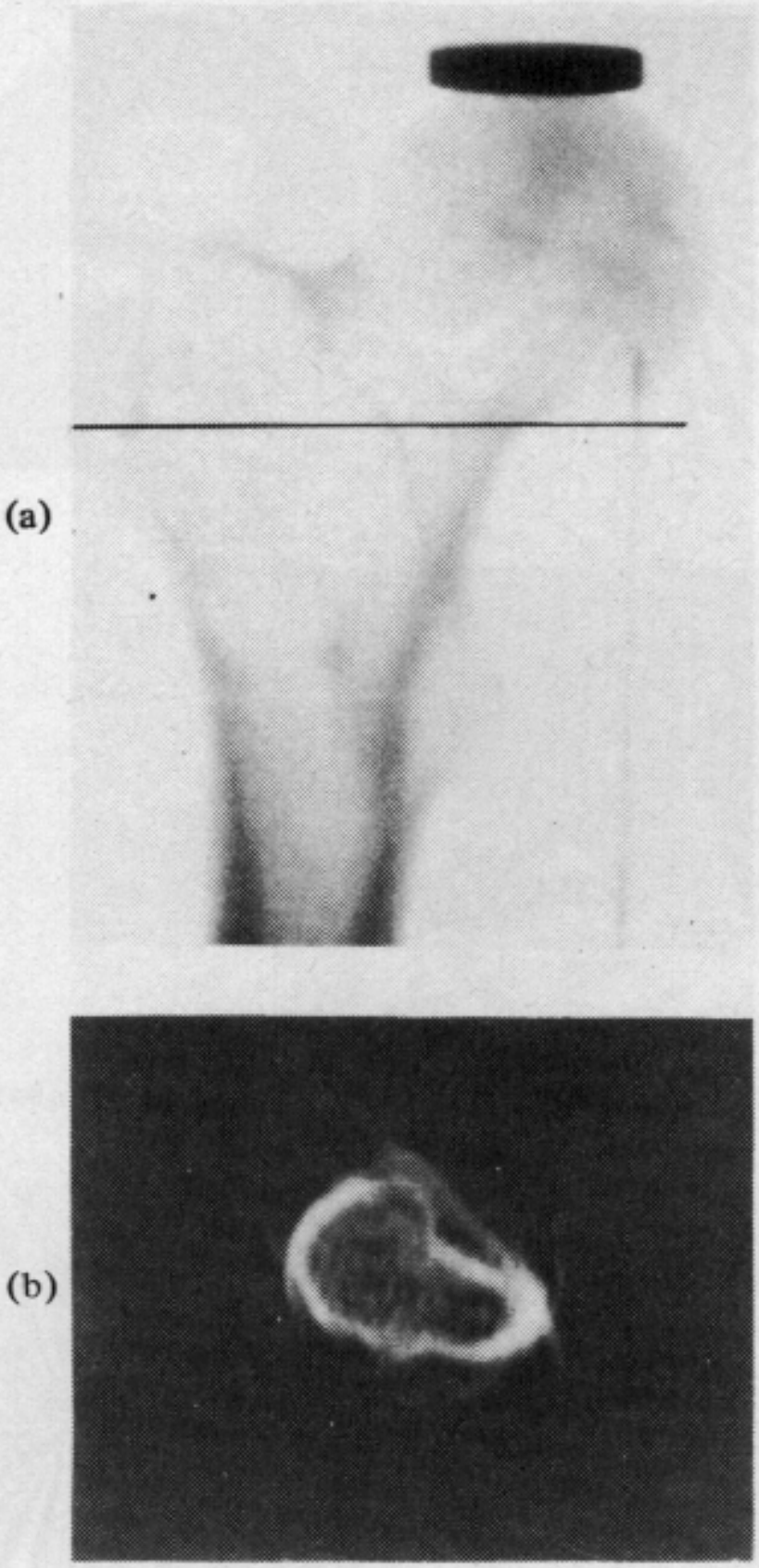

Fig. 21. Reconstruction from a series of X-rays of an excised human femur using the concentric-squares linear interpolation algorithm. (a) One of the set of X-rays. (b) Reconstruction of cross section at the level of the dark line indicated in Fig. 21(a).